Acta Biomaterialia 151 (2022) 317–332

Contents lists available at ScienceDirect

Acta Biomaterialia

journal homepage: www.elsevier.com/locate/actbio

Full length article

Modelling transcranial ultrasound neuromodulation: an energy-based multiscale framework

Haoyu Chen[a], Ciara Felix[a], Davide Folloni[b,c], Lennart Verhagen[b,e], Jérôme Sallet[b,d], Antoine Jerusalem[a,*]

[a] Department of Engineering Science, University of Oxford, Oxford, UK
[b] Wellcome Centre for Integrative Neuroimaging (WIN), Department of Experimental Psychology, University of Oxford, Oxford, UK
[c] Department of Neuroscience and Friedman Brain Institute, Icahn School of Medicine at Mount Sinai, New York, NY, USA
[d] Inserm, Stem Cell and Brain Research Institute, Université Lyon 1, Bron, France
[e] Donders Institute, Radboud University, Nijmegen, Netherlands

ARTICLE INFO

Article history:
Received 8 February 2022
Revised 18 July 2022
Accepted 19 July 2022
Available online 25 July 2022

Keywords:
Cell multiphysics
Neuromodulation
Transcranial ultrasound stimulation
Neuron computational models

ABSTRACT

Several animal and human studies have now established the potential of low intensity, low frequency transcranial ultrasound (TUS) for non-invasive neuromodulation. Paradoxically, the underlying mechanisms through which TUS neuromodulation operates are still unclear, and a consensus on the identification of optimal sonication parameters still remains elusive. One emerging hypothesis based on thermodynamical considerations attributes the acoustic-induced nerve activity alterations to the mechanical energy and/or entropy conversions occurring during TUS action. Here, we propose a multiscale modelling framework to examine the energy states of neuromodulation under TUS. First, macroscopic tissue-level acoustic simulations of the sonication of a whole monkey brain are conducted under different sonication protocols. For each one of them, mechanical loading conditions of the received waves in the anterior cingulate cortex region are recorded and exported into a microscopic cell-level 3D viscoelastic finite element model of a neuronal axon embedded in extracellular medium. Pulse-averaged elastically stored and viscously dissipated energy rate densities during axon deformation are finally computed under different sonication incident angles and are mapped against distinct combinations of sonication parameters of the TUS. The proposed multiscale framework allows for the analysis of vibrational patterns of the axons and its comparison against the spectrograms of stimulating ultrasound. The results are in agreement with literature data on neuromodulation, demonstrating the potential of this framework to identify optimised acoustic parameters in TUS neuromodulation. The proposed approach is finally discussed in the context of multiphysics energetic considerations, argued here to be a promising avenue towards a scalable framework for TUS in silico predictions.

Statement of significance

Low-intensity transcranial ultrasound (TUS) is poised to become a leading neuromodulation technique for the treatment of neurological disorders. Paradoxically, how it operates at the cellular scale remains unknown, hampering progress in personalised treatment. To this end, models of the multiphysics of neurons able to upscale results to the organ scale are required. We propose here to achieve this by considering an axon submitted to an ultrasound wave extracted from a simulation at the organ scale. Doing so, information pertaining to both stored and dissipated axonal energies can be extracted for a given head/brain morphology. This two-scale multiphysics energetic approach is a promising scalable framework for in silico predictions in the context of personalised TUS treatment.

* Corresponding author.
E-mail address: antoine.jerusalem@eng.ox.ac.uk (A. Jerusalem).

https://doi.org/10.1016/j.actbio.2022.07.034
1742-7061/

1. Introduction

In the past decade, low intensity, low frequency transcranial ultrasound (TUS) has emerged as a new technique to modulate neuronal activities with high spatial precision and penetration depth [1,2]. When compared with other neuromodulation approaches such as electroconvulsive therapy, vagus nerve stimulation, transcranial magnetic stimulation and deep brain stimulation, TUS-mediated neuromodulation has superior advantages, such as being non-invasive, low-cost and bi-modal, i.e., possessing the capability to both excite and suppress nerve activity [2,3]. At the tissue/organ level, compelling evidence of TUS-mediated neuromodulatory effects, mainly demonstrated through functional magnetic resonance imaging (fMRI), electroencephalography (EEG), near-infrared spectroscopy (NIRS) and sensory or motor behaviours, has been reported in both human and animal studies [2,4–12]. At the cellular level, ultrasound has been shown to mediate membrane potential in both neurons and oocytes through cell membrane deflection [13] or cell activity modulation, e.g., altering currents flowing through the ion channels, activating mechanosensitive ion channels, initiating calcium influx, increasing specific gene expression in cell nucleus, as well as increasing the spontaneous firing rate [14–21]. Paradoxically, the underlying micromechanisms under which TUS neuromodulation operates still remain mostly unknown, though different theories have already been proposed, e.g., sonoporation and cavitation, acoustic radiation force, flexoelectricity, thermodynamic pulses, among others [5,6,22–25]. In addition to this, the stimulation protocols used in TUS, involving the choice of natural frequency (NF) and pressure, duty cycle (DC), pulse repetition frequency (PRF) and sonication duration, diverge immensely across literature studies [23,26]. While some pioneering studies have been conducted on the identification of optimal values [27–31], their conclusions disagree with each other. A consensus on the optimisation of sonication parameters and the standardisation of the stimulation protocols is thus needed for TUS to fully establish itself as a reliable and interpretable clinical tool.

Recently, an increasing body of research has reconsidered the nature of action potential (AP) as a multiphysics phenomenon, thus casting new light on the mechanisms of TUS action from a thermodynamic perspective [22,24,32,33]. In such approach, the cell membrane is considered as a thermodynamic system whose internal physical properties are reciprocally coupled [34–37]. The membrane has an equilibrium state, and can transform into other conformations when perturbed. During this phase change, exchanges of intertwined physical properties, such as enthalpy and entropy, occur following thermodynamic laws. During AP propagation, this whole process is reversible as the membrane naturally returns to its equilibrium state [24]. Under this paradigm, the mechanism of TUS action can be viewed as: low intensity ultrasound modulates cell activity by transferring mechanical energy into the membrane, resulting in a membrane pressure wave which may either directly activate mechanosensitive ion channels or indirectly perturb the membrane thermodynamic equilibrium [24].

In the last decade, research groups have conducted numerical studies to investigate the response of neuronal membrane under ultrasound stimulation, with focus on its electrophysiological feedback [13,29,31,38–44]. Compared with experimental studies, promising results have been predicted using these numerical models, such as effective membrane oscillation, ultrasound-induced capacitive current and membrane polarisation. However, the geometries used in these studies are mostly formulated in one dimension or can be simplified to one dimension mathematically. In addition, only idealised waveforms (no wave interference or superposition in the brain is considered) are used for the ultrasound profile and none of these studies have scrutinised the energy states of the cell membrane. In this study, we propose a 3D modelling framework which simulates cell-level mechanical response of neuronal axons (such as local membrane vibrations and deformations) under realistic local acoustic pressure perturbations, computed directly from the simulation of transcranial ultrasound waves in monkey TUS neuromodulation using different sonication protocols. It is shown here that this modelling framework can be used to link cell-level energy state due to acoustic stimulation to tissue-level ultrasound sonication parameters. In addition, it can be used to evaluate the microscopic vibration patterns of the neurons and compare those with the vibration features of the driving acoustic waves. In the following section, the overall multiscale methodology is presented, followed by the simulation results and a discussion, particularly focused on the thermodynamic implications of this work.

2. Modelling methodology

2.1. Overview

Figure 1 shows the two scales of the proposed modelling framework: the macroscopic tissue scale (Figure 1 (a)) and the microscopic cell scale (Figure 1 (b)). At the macroscopic scale, the framework uses a macroscopic model (MaM) that simulates acoustic wave propagation in a monkey brain whose geometry is constructed from monkey head image segmentations, whereas, at the microscopic scale, the framework uses a microscopic model (MiM) that models the local vibration and deformation of the cell embedded in an extracellular matrix (ECM) under acoustic waves. Details of our modelling framework are summarised in the following subsections.

2.2. The macroscopic model - MaM

In the MaM, a 3D monkey head model is generated from the segmentation of in vivo structural MRI data, obtained from both hemispheres of a rhesus monkey (Macaca mulatta, female) using a 3T MRI Siemens scanner, see Ref. [45] for more details. Voxels of $0.5 \times 0.5 \times 0.5\,\mathrm{mm}^3$ in size are used in the MRI scan, see Figure 2(a). Scanned raw images are segmented using data visualisation software Amira (Thermo Scientific, Waltham, MA, United States). Figure 2(a) also shows the segmented head consisting of ten distinct parts illustrated using different colours, including the white matter, the grey matter, the ventricles, the brainstem, the falx cerebri, the cerebellum, the skull, the cerebrospinal fluid, and other soft tissues (muscles, skin, fat, etc.). The segmented Amira image file is then reconstructed into the monkey head model in a matrix format using MATLAB (Natick, MA, United States), see Figure 2(b). Voxels were further discretised to smaller ones of $0.25 \times 0.25 \times 0.25\,\mathrm{mm}^3$ to allow for simulations of higher frequencies.

To model ultrasound propagation in the head model, the open source MATLAB acoustics toolbox k-Wave [46] is used. k-Wave calculates the instantaneous pressure field in the skull during acoustic propagation by solving the three first-order acoustic equations (motion, continuity and state):

$$\frac{\partial \mathbf{u}}{\partial t} = -\frac{1}{\rho_0}\nabla p \tag{1a}$$

$$\frac{\partial \rho}{\partial t} = -\rho_0 \nabla \cdot \mathbf{u} \tag{1b}$$

$$p = c^2 \rho \tag{1c}$$

where $\mathbf{u}$ is the acoustic particle velocity, ρ_0 is the ambient density, ρ is the acoustic density, c is the thermodynamic sound speed, p is the acoustic pressure.

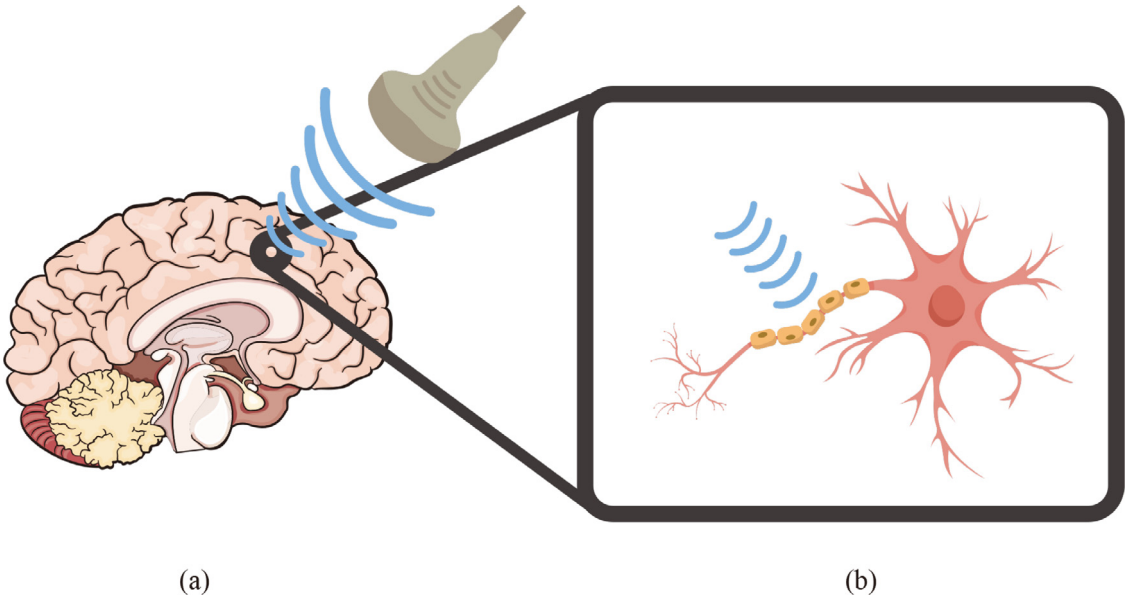

Fig. 1. Graphical representation of the framework. (a): At the macroscopic scale, the macroscopic model (MaM) simulates acoustic wave propagation in the brain. (b): At the microscopic scale, the microscopic model (MiM) models the local vibration and deformation of the cell embedded in an ECM arising from the acoustic waves.

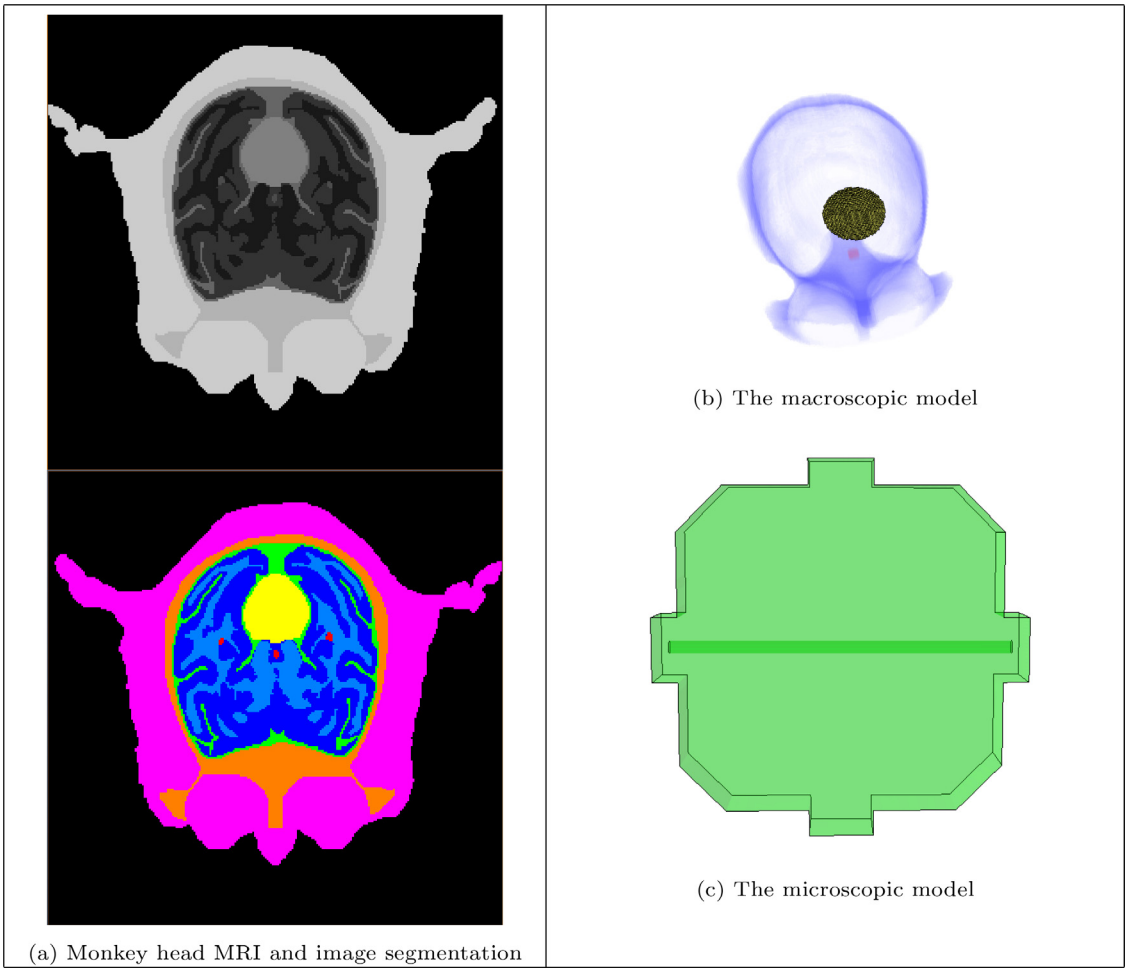

Fig. 2. Illustration of the modelling framework. (a): Monkey head MRI and image segmentation. (b): Macroscopic model; monkey head reconstruction and placement of the acoustic source. The focal zone resides in the anterior cingulate cortex of the brain (shown as the red spot). (c): Microscopic model; finite element modelling of axon embedded in the extracellular fluid.

Table 1
Mechanical properties of different brain parts used in the macroscopic model simulations [45].

Brain parts	Medium density (kg/m^3)	Medium sound speed (m/s)
White matter	1030	1600
Grey matter	1050	1550
Ventricles	1006	1515
Brainstem	1030	1558.5
Falx cerebri	1133	1558.5
Cerebellum	1030	1537
Cerebrospinal fluid	1006	1515
Skull	1912	3700
Flesh	1059	1440
Amygdala	1133	1558.5
Anterior cingulate cortex	1020	1558.5

In the k-Wave toolbox, an external acoustic source is placed over the head, representing a single element concave transducer with 64 mm outer diameter and 64 mm radius of curvature, commonly used in experimental studies of ultrasound neuromodulation. The focal zone of the acoustic source resides in the head anterior cingulate cortex region (the red spot in Figure 2(b)). To determine the range of sonication parameters used in this model, we have summarised the sonication protocols of all experimental studies on TUS neuromodulation of monkeys in the literature to our best knowledge, including Ref. [4,47–57]. We excluded some parameters which are clearly far beyond the normal range used in other studies and concluded that, among most of these studies, frequency ranges between 250 kHz and 800 kHz; PRF ranges between 500 Hz and 2 kHz; duty cycle ranges between 30% and 100% where 100% stands for continuous wave; pressure ranges between 0.35 MPa and 1.74 MPa and sonication duration ranges between 100 ms and 300 ms. In order to investigate the influences of NFs and PRFs, we set up the acoustic source in our simulation as follows: pulsed sinusoidal ultrasound waves are applied with constant sonication duration (2 ms), constant pressure amplitude (1.35 MPa) and DC (50%), but different combinations of NFs and PRFs. The NF is varied from 250 kHz to 650 kHz, whereas PRF varies from 500 Hz to 2, 000 Hz. In addition, a sensor marker is also placed inside the focal zone to collect values of the time varying local pressure field. Mechanical properties of different brain parts used in the simulations are obtained from the literature [45], see Table 1. The 3D computational domain was discretised to voxels of $0.25 \times 0.25 \times 0.25\,\text{mm}^3$ with a total number of $512 \times 512 \times 256$ grid points in all x-, y- and z-directions. Equation (1) is numerically solved on these grid points using the pseudo-spectral and k-Space methods (see Ref. [46] for more details). Finally, values of the time-varying pressure field of the received waves of different combinations of frequency and PRF are recorded at every time step and exported into the MiM as pressure boundary conditions.

2.3. The microscopic model - MiM

2.3.1. Model description

The MiM simulates the vibration and deformation of an axon filled with axoplasm embedded in an ECM, subjected to a realistic pressure wave. This work focuses on axons (though applicable to any neurite) for two main reasons. The first is to simplify the introduction of the proposed framework; somas are of various shapes and sizes while the geometry of the axon allows for an easier generalisation of the results presented in this work. The second is based on the recent results by the authors demonstrating the leading role of white matter tracts leaving a sonicated region in a quasi-identical context [45]. It must however be noted that other extensions of this work using other neuronal geometries are readily achievable. This model is built using the finite element package Abaqus (Dassault Sysèmes SE, Vélizy-Villacoublay, France). The coupled Eulerian-Lagrangian approach is adopted to model the interaction between the axon and the extracellular fluid as well as the axoplasm. A special geometry is designed for this model: the idealised axon is modelled as a long hollow cylindrical tube with a length L of 550 μm, a diameter D of 5 μm and a membrane thickness H of 5 nm. Since the mechanical contribution of myelination in vivo is not straightforward to evaluate, we follow the approach described in Ref. [40] and do not differentiate myelinated and unmyelinated axons in MiM. The axon is embedded in a surrounding homogenised ECM which is modelled as a fluid box of octagonal prism shape of 500 μm edge length and 100 μm thickness (see Figure 2(c)). The choice of this particular shape is to facilitate the simulation of acoustic waves incoming from different sonication incident angles (SIAs) with respect to the axon, as well as to enable modelling inhomogeneous deformations in the axon due to local interactions between the solid and fluid (as planar waves result in homogeneous deformations in the axon). Finally, the axial displacement of both ends of the axon is constrained, while the other degrees of freedom are set to remain free so that a significant portion of the axon is subjected to the wave, while not being free to fully move axially as one would expect from real white matter.

In literature experiments, axons are observed to exhibit elastic response, viscoelastic relaxation as well as active contraction during mechanical tests [58,59]. Their physical properties may influence the propagation (elastic) or attenuation (viscous) of mechanical signals across the cell membrane [60]. Therefore, to capture the viscoelastic response of the axon, a linear viscoelastic material model is adopted. In particular, the axon is modelled using a two-branch Generalised Maxwell model, which consists of one long-term elastic branch (spring), in parallel with one viscous branches (spring and dashpot) in series. Prony series notations are used to describe this mechanical model. The relaxation time τ of the viscous branch is defined as $\tau = \nu/G_\nu$, where ν is the viscosity of the dashpot and G_ν is the shear modulus of spring in the viscous branch. The long term shear modulus G_∞ of the elastic branch corresponds to the elastic response of the material once it is totally relaxed.

When modelling very fast material response under high pressures, such as the hydrodynamic behaviour of axoplam or ECM under shock waves at a given temperature, the volumetric part of the stress tensor can be described by an equation of state [61,62]. The Hugoniot/Mie-Grüneisen equation of state, which assumes a linear relationship between the shock velocity U_s and the particle velocity U_p [63], is a popular candidate, i.e.:

$$U_s = c_0 + sU_p \tag{2}$$

where c_0 and s are material parameters which can be obtained from experiments. This equation of state is adopted to model the volumetric part of the constitutive relation of ECM. Making use of Equation (2) and the equations of conservation of mass and momentum in a control volume at the shock front, the Hugoniot pressure p_H can be calculated as a function of the nominal volumetric compressive strain η and the reference density ρ_0:

$$p_H = \frac{\rho_0 {c_0}^2 \eta}{(1 - s\eta)^2} \tag{3}$$

where η is defined using the current density ρ and the reference density ρ_0:

$$\eta = 1 - \frac{\rho_0}{\rho} \tag{4}$$

In addition, it is also possible to relate the pressure p (defined here as positive in compression) and the internal energy per unit mass

Table 2
Geometrical and mechanical parameters of the axon, axoplasm and ECM used in the microscopic model.

Axon geometries		
Axon length	L	550 μm
Axon diameter	D	5 μm
Membrane thickness	H	5 nm
Axon mechanical properties		
Membrane density	ρ	1050 kg/m^3
Poisson's ratio	ν	0.49
Long term shear modulus	G_∞	50 Pa
Viscous branch shear modulus	G_ν	280 Pa
Viscoelastic relaxation time	τ	10 ms
Axoplasm and ECM mechanical properties		
Density	ρ_0	1000 kg/m^3
Speed of sound	c_0	1550 m/s
Material parameter	s	1.99
Grüneisen ratio	Γ_0	0.1
Dynamic Newtonian viscosity	μ	0.001 Pa · s

E_m to their respective values on the Hugoniot curve p_H and E_H using the Mie-Grüneisen equation of state [63], which leads to

$$p = \frac{\rho_0 {c_0}^2 \eta}{(1-s\eta)^2}\left(1 - \frac{\Gamma_0 \eta}{2}\right) + \Gamma_0 \rho_0 E_m \tag{5}$$

where Γ_0 is the Grüneisen ratio in the initial state and is a material constant. The rate of internal energy $\dot{E}_m$ is given by the first law of thermodynamics and is calculated as the sum of the volumetric and deviatoric ($\dot{\Psi}_{dev}$) free energy rates, and heat rate $\dot{Q}$ [61], i.e.:

$$\dot{E}_m = -\frac{1}{\rho}\left(\frac{p\dot{\rho}}{\rho} + \dot{\Psi}_{dev}\right) + \dot{Q} \tag{6}$$

For low intensity transcranial pulsed ultrasound, its thermal effect on the brain tissue is likely negligible (often $< 0.1^\circ$CC) [2,24,64], hence it is reasonable to consider the whole propagation process to be adiabatic, i.e., $\dot{Q} = 0\,\mathrm{J/(kg \cdot s)}$. The deviatoric contribution of the fluid stress tensor is assumed to follow the dynamic Newtonian viscosity μ of water.

Material parameters used in this MiM are summarised in Table 2. Mechanical parameters of the axon are calibrated by simultaneously nonlinear-least-square fitting the equivalent storage and loss moduli of a two-branch Generalised Maxwell model at different frequencies to the frequency-dependent rheological properties of neurons experimentally measured in Ref. [65]. Mechanical parameters of the ECM are obtained directly from literature studies [61].

In order to stabilise the simulation, an artificial viscosity formulation is also included in the model. This increases the stability of elements at highest frequencies and prevent them from collapsing under extremely high velocity gradients. To be specific, an artificial bulk viscosity (p_{bv}) is added to the pressure term, which is composed of a linear and a quadratic term:

$$p_{bv} = b_1 \rho c_d L_e \dot{\epsilon}_{vol} + \rho (b_2 L_e \dot{\epsilon}_{vol})^2 \tag{7}$$

where b_1 and b_2 are damping coefficients, L_e is the characteristic element size, ϵ_{vol} is the volumetric strain and c_d is the dilatational wave speed. This artificial viscosity formulation is already implemented in Abaqus, and no additional subroutine implementations is needed. In this study, we have chosen values of $b_1 = 0.06$ and $b_2 = 1.2$. The strain energy density arising from this 'artificial' additional constraint was averaged for the eight elements in the region of interest. At least one order of magnitude lower between this resulting value and the other energy density forms of the problem (elastic stored and viscous) was observed, thus ensuring that the physics of the problem was conserved when attenuating the spurious modes arising from the discretisation.

2.3.2. Model analysis

In order to quantify the energy transfer rate from the acoustic wave to the axon, we make use of two quantities: the pulse averaged elastic energy rate density (PAEERD) and the pulse averaged viscous energy rate density (PAVERD) of the axon, both defined over one pulse period T:

$$\mathrm{PAEERD} = \frac{1}{T}\int_0^T \dot{\Psi}_e(t)\,\mathrm{d}t \tag{8a}$$

$$\mathrm{PAVERD} = \frac{1}{T}\int_0^T \dot{\Psi}_\nu(t)\,\mathrm{d}t \tag{8b}$$

where Ψ_e is the total elastic strain energy density stored in the material per unit membrane area A, and Ψ_ν is the total viscous energy density dissipated in the material due to material viscosity per unit membrane area A [31]. $\dot{\Psi}_e$ and $\dot{\Psi}_\nu$ are defined for each shell element as:

$$\dot{\Psi}_e(t) = \frac{1}{A_e}\iiint_{V_e}\left(\boldsymbol{\sigma}_\infty : \dot{\boldsymbol{\epsilon}} + \boldsymbol{\sigma}_\nu : \frac{d}{dt}(\boldsymbol{\epsilon} - \boldsymbol{\epsilon}_\nu)\right)\mathrm{d}x\mathrm{d}y\mathrm{d}z \tag{9a}$$

$$\dot{\Psi}_\nu(t) = \frac{1}{A_e}\iiint_{V_e}\boldsymbol{\sigma}_\nu : \dot{\boldsymbol{\epsilon}}_\nu\,\mathrm{d}x\mathrm{d}y\mathrm{d}z \tag{9b}$$

where A_e is the shell element area, V_e is the shell element volume (with $V_e = A_e \times H$ where H is the element thickness), $\boldsymbol{\sigma}_\infty$, $\boldsymbol{\sigma}_e$ and $\boldsymbol{\sigma}_\nu$ are the elastic and viscous branches elastic stress tensors and viscous stress tensor, respectively, and $\boldsymbol{\epsilon}$ and $\boldsymbol{\epsilon}_\nu$ are the strain tensor and viscous strain tensor. Both PAEERD and PAVERD are expressed in the unit of watts per square centimetres (W/cm^2). Physically, PAEERD relates to the spatial peak pulse average intensity (I_{SPPA}) of acoustic wave that is locally transformed into axon vibration during ultrasound brain neuromodulation, whereas PAVERD relates to the rate density of the energy that has been dissipated during this transformation. In our model, representative values of PAEERD and PAVERD are evaluated by averaging the values of PAEERD and PAVERD of all the finite elements in a region of interest (RoI) defined by 16 elements localised in the middle of the axon (with two circumferential rows of 8 elements).

In this finite element model, the axon is discretised with triangular linear shell elements, whereas the ECM is discretised with linear eulerian brick elements with reduced integration and hourglass control. For modelling ECM-axon-axoplasm interaction, a contact algorithm is defined between the Eulerian mesh (fluid) and the Lagrangian mesh (solid), in which a 'hard' contact is chosen for the normal direction, coupled to a penalty tangential friction formulation with a friction coefficient of 0.3. A mesh size of 1 μm in the axonal neighbourhood is chosen as a good compromise between convergence and calculation time. For each sonication condition (NF and PRF), the local time varying pressure evolution measured in the MaM is applied on one side face of the fluid box as the loading boundary condition. This loading boundary condition is applied on three different side faces to simulate incoming wave from 0°, 45° and 90° SIAs with respect to the axon main axis. In addition, in order to minimise the internal reflection of dilatational and shear wave energy back into the computational domain, non-reflecting boundary conditions are applied on all other sides of the fluid box. Explicit dynamic simulations are run for each case of imposed boundary conditions for 2 ms. Variables, including PAEERD and PAVERD of the RoI, are extracted for analysis.

Spectrogram analysis is a common tool used to analyse the spectrum of a signal as its frequency decomposition varies with time. To quantitatively examine how the axon vibration pattern is affected by its acoustic driving pressure and whether factors such as PRF and the presence of extracellular fluid may have an impact, spectrogram analyses are performed for the RoI. Instantaneous motions of the axon are decomposed into orthogonal directions, and

kinetic quantities such as cross section deformations are extracted and transformed into the frequency domain. Spectrogram analyses are performed by dividing the signal into segments and applying windowing in each segment with a Hamming window of segment length. This is done in MATLAB using a customised code. Finally, the vibration (diameter alteration) spectrograms of the axons are compared with the spectrograms of the driving acoustic waves' pressure. The in-plane diameter (vertical in the figure) of the axon is considered here.

3. Results

3.1. Acoustic simulation of the brain

The following results are obtained from the simulations with pulsed sinusoidal acoustic waves of constant pressure amplitude (1.35 MPa) and DC (50%), but different combinations of NFs (250 kHz, 450 kHz and 650 kHz) and PRFs (500 Hz, 1000 Hz and 2, 000 Hz). All simulations are of 2 ms sonication duration.

Figure 3 shows the evolutions of the initial intracranial pressure map during the propagation of three ultrasound waves of different protocols through the monkey brain (PRF = 1, 000 Hz; NF = 250 kHz, 450 kHz and 650 kHz). Pressure map snapshots were taken at three different time points: 30 μs, 60 μs and 90 μs. In order to illustrate the initial pressure distribution, these time points are intentionally chosen to be located within the 'on' phase of the first pulse of these acoustic waves. In other words, the parameter PRF plays no role in these cases and changing the PRF will not affect the pressure maps. In these simulations, as the time increases, the ultrasound wave propagates outward from the sensor through the entire brain. Acoustic focal zones can be also observed, though local pressure concentration exists in other regions outside the focal zones as well. The initial pressures in the low frequency case (250 kHz) are at least one order of magnitude higher than that for its high frequency (450 kHz and 650 kHz) counterparts (note that the colorbar scale of the first row is different from those of the last two rows). These discrepancies may be explained by a higher energy dissipation for high frequency than for low frequencies.

Figure 4 shows the evolution of intracranial pressure measured at the sensor position under different stimulation protocols. In addition to the 'on' and 'off' effect of the acoustic waves, waveforms are the results of the superposition and interference of the waves reflected inside the head, thus leading to rather complicated patterns as opposed to a simple sinusoidal form. From this figure, it can be seen that for low frequency cases (250 kHz), the waveforms have already entered a steady state, whereas for high frequency cases (450 kHz and 650 kHz), these waveforms might still seem to be within a transient regime; or, at the very least, the steady state regime is more difficult to identify. This is mainly due to the fact that the complexity and heterogeneity of the brain anatomy both increase the time for interfered waves to enter the steady-stage propagation (when at all). In addition, it can also be observed that as the NF increases, the sensor maximum pressure decreases. Finally, it is worth noting that the sensor maximum pressure reaches 1.9 MPa for 250 kHz case which is higher than the pressure of the acoustic source, whereas it is only approximately 0.6 MPa for the 650 kHz cases.

3.2. Finite element simulation of the axon

Figure 5 shows the colourmaps of PAEERD and PAVERD computed in the middle of the axon when subjected to local pressure waves of different sonication incident angles (0°, 45° and 90°) in the MiM at 2 ms. These figures show that, for one simulation, the magnitude of PAEERD is one to two orders of magnitude higher than the PAVERD, which indicates that, locally, most of the energy carried by the pressure wave is transformed into elastic energy in the axon, rather than being dissipated. However, this dis-

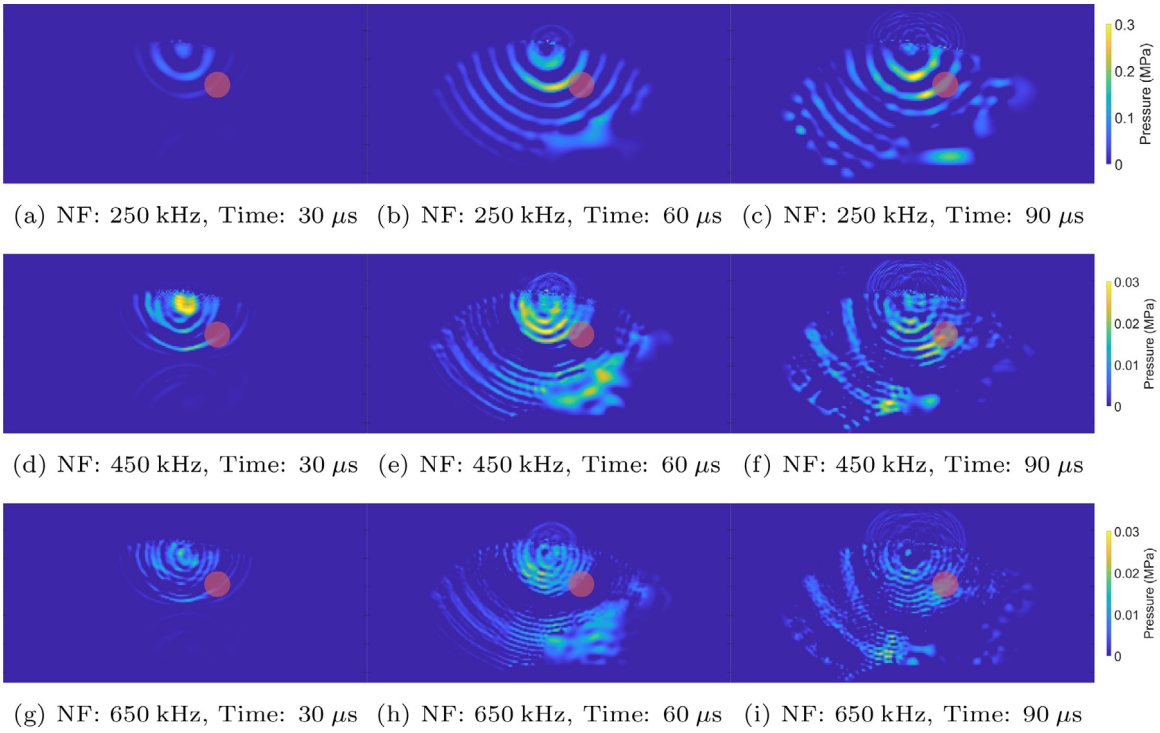

(a) NF: 250 kHz, Time: 30 μs (b) NF: 250 kHz, Time: 60 μs (c) NF: 250 kHz, Time: 90 μs

(d) NF: 450 kHz, Time: 30 μs (e) NF: 450 kHz, Time: 60 μs (f) NF: 450 kHz, Time: 90 μs

(g) NF: 650 kHz, Time: 30 μs (h) NF: 650 kHz, Time: 60 μs (i) NF: 650 kHz, Time: 90 μs

Fig. 3. Evolutions of the intracranial pressure during the propagation of ultrasound waves of different natural frequencies (NFs) through the brain (sagittal section showed here) as predicted by the macroscopic model. Snapshots are obtained at three different time points: 30 μs, 60 μs and 90 μs. Geometrical focus of the transducer is indicated with a red spot in each sub-figure. Note that the colormap scales of the first row (NF: 250 kHz) is one order of magnitude higher than those of the second (NF: 450 kHz) and the third (NF: 650 kHz) rows.

sipated energy cannot be neglected, as its accumulation eventually contributes to the attenuation of the acoustic energy as the wave propagates. In addition, it must be emphasised that the NF has a much larger influence on the values of PAEERD and PAVERD than the PRF. Interestingly, as the SIA increases, PAEERD also increases. For cases in which the incident angle is zero (wave propagation direction is parallel to the axon axis), the magnitudes of PAEERD and PAVERD are much lower than other cases. This may be because, in this particular situation, the pressure waves are actually pushing one end of the axon. And since the contact area between the pressure wave and the axon in this case (only through axon membrane thickness) is much smaller than in other cases where pressure waves directly impinge on the surface of the membrane, the mechanical energy absorbed by the axons is also much lower.

The present simulations were not able to clearly capture the transverse "wobbling" effect expected in the case SIA=0° (arising from the Poisson effect) as was seen in Ref. [40]. In the present study, both MiM axoplasm and extracellular fluid interact with the axon membrane acting as lateral constraints. In comparison with the model in Ref. [40] which did not incorporate any fluid (just a solid model), these fluid constraints confine the membrane movement and increase indirectly the membrane stiffness, thus potentially affecting any transverse wave propagation. As the axon geometry in the MiM is much shorter than that in Ref. [40], a different behaviour is indeed expected in this new model, thus potentially complementing the previous study.

3.3. Vibrational analyses of the axon

Figure 6 shows how the axon deforms under the action of acoustic pressure waves (with the right insets showing the middle cross section of the axon) in the MiM for NF= 450 kHz, PRF= 500 Hz, SIA = 90° at (a) 0 ms; (b) 0.445 ms; (c) 0.668 ms. In this particular example, the waves propagates downwards and impinges perpendicularly on the axon surface, resulting in vertical vibration of the axon (bending) and a periodical deformation of the cross section.

Figure 7 shows the spectrogram analysis of the local pressure waves shown in Figure 4, as well as the spectrogram analysis of the axon vibration subjected to these pressure waves (characterised by the alterations of axon middle section diameter), under different combinations of NFs and PRFs. In this analysis, we only consider cases in which SIA = 90°, i.e., waves propagate perpendicularly downwards (waves of other SIAs deform the axon cross section laterally too, making the projection results difficult to be interpreted). In each subfigure of Figure 7, the upper row is the pressure wave spectrogram whereas the lower row is the axon vibration spectrogram. Note that the vertical bright yellow lines in these figures are artefacts due to the 'on/off' of the ultrasound (i.e., corresponding to the PRF and DC of the acoustic pulses). The results shows that axons vibrate in a complex pattern under acoustic waves. In the spectrograms of the axon vibration, a band can be observed which corresponds to the band of same frequency in the spectrogram of its triggering pressure wave, indicating a forced vibration roughly in phase with the pressure wave. For NF=250 kHz, the vibration band is less clear (particularly at low PRF) and seems to interferes with a much lower frequency mode. This second frequency band, which is brighter (indicating oscillations with much larger amplitudes), also exists at a much lower frequency (close to zero) for all NF/PRF combinations, likely related to the natural resonance frequency of the axon itself. This natural resonance frequency of the axon is determined by the axon geometry, material properties, the Newtonian damping due to fluid viscosity, as well as axon-fluid contact criterion (for example, no slip contact will be different from frictionless contact). As the NF and PRF increase, the vibration patterns become clearer and both frequency bands dissociate clearly. However, the higher the NF of the pressure wave is, the weaker the axon vibrates and the more its vibration is dominated by its own resonance. In high NF regimes, changing the PRF of the triggering pressure wave does not seem to have much effect on the vibration pattern of the axons.

4. Discussion

4.1. Reliability and validity of MaM results

In the past decade, simulation of transcranial ultrasound have been systematically conducted on 3D head models of both humans and animals to examine the intracranial acoustic pressure map during ultrasound propagation [28,49,50,66–73]. More specifically, in silico models have allowed to study the effect of the position of the acoustic transducer along with its sonication parameters (such as pressure magnitude and frequency) on the temporal change and spatial distribution of the resulting intracranial acoustic pressure for a given skull morphology. While these models have allowed for very accurate predictions, assumptions on brain material properties or even the linearity of the acoustic propagation model are required. A first step for our model is thus to ensure that the acoustic pressure measured in the MaM simulations is meaningful and realistic before it can be used for the subsequent MiM simulations. Sensitivity studies showed that the impact of acoustic medium properties on the simulated transcranial ultrasound fields is substantial, in which sound speed (depending on the brain material properties) is shown to be the dominant acoustic property [74]. Assuming homogeneous brain medium properties results in an imprecise result compared to the case in which proper heterogeneous properties are used [68,75]. In addition, small alterations in the skull geometry (such as geometry being obtained from low resolution images and being smoothed) may result in significant changes in the acoustic pressure map. However, it seem that using nonlinear acoustic model for TUS simulation is virtually identical to the linear case in terms of pressure distribution [68]. Technically speaking, the major difficulty of validating the MaM simulation results is that direct measurements of acoustic pressure level in an intact head (i.e., with full skull and brain tissue) during ultrasound propagation is not possible. Instead, in situ intracranial acoustic pressure levels have been measured alternatively by using a hydrophone in a skull-hydrogel experimental model (or simply water) in a water tank [28,69,71]. For similar values of sonication parameters and transducer placement, our simulation results show that the pressure levels computed in our MaM simulations fall within the experimentally estimated range observed in experimental studies on monkeys, and are in good agreement with simulation results of other studies [66,68].

4.2. Mechanical models in MiM and modelling neurons' mechanical responses

In the MiM, a two-branch linear viscoelastic model is used as a first order approximation for the axon's material constitutive model, while the Mie-Grüneisen equation of state is used to model the axoplasm and extracellular matrix. The former has commonly been adopted in cell biomechanics studies [76–78] when the deformation of the cell is small. The deformation was monitored in all simulations and an absolute value of about 15%-20% was found for the maximum principal strain of the axon membrane (accounting for the contribution of both elastic and viscous strains), with most of the axon remaining below 5%. This means that the maximum elastic strain is, at worst, borderline leaving the linear regime, while most of the axon remains in the linear regime. Furthermore, the main aim of our paper is to propose a potential methodology to investigate the optimised sonication param-

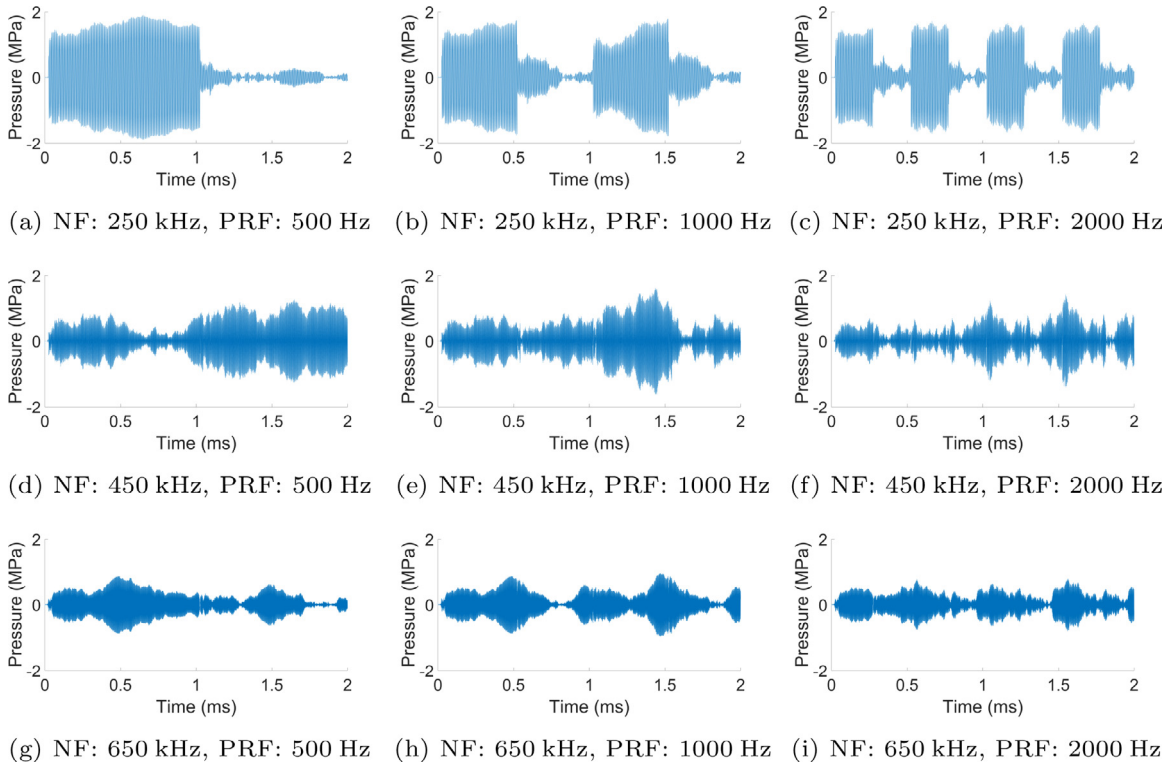

Fig. 4. Temporal evolution of the intracranial pressure measured at the sensor position under different stimulation protocols. Each row corresponds to the same natural frequency (NF), whereas each column has the same pulse repetition frequency (PRF).

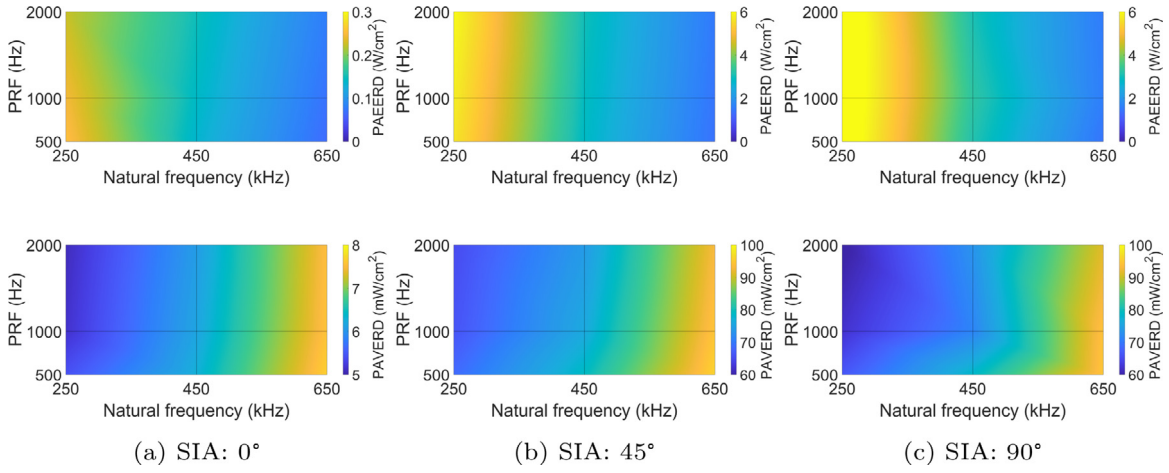

Fig. 5. Maps of PAEERD and PAVERD at the axon centre subjected to local pressure waves against the natural frequencies and pulse repetition frequencies (PRFs) of the acoustic source in the macroscopic model for different sonication incident angles (SIAs) in the microscopic model at 2 ms.

eters used in TUS from an energetic perspective, while acknowledging that more accurate models of the axon, ECM, etc. could be used for specific organ locations and species. In reality, cells usually demonstrate nonlinear behaviours under mechanical loading conditions leading to large deformation [79–81]. Linear viscoelasticity may thus not be able to accurately predict the finite strain response of the cells membrane when the cell deformation exceeds the linear regime and, in this case, nonlinear viscoelasticity ought to be considered. The Mie-Grüneisen equation of state relates the pressure to the volume of a condensed material at a given temperature. Therefore, it is usually used to model materials at high pressure. However, the Mie-Grüneisen equation of state is also applicable to hydrodynamic behaviours at lower pressures. In fact, it is one of the a few major material models that is commonly applied to define an incompressible inviscid fluid (such as water); with others including modelling water as a quasi-elastic medium with small Young's modulus and 0.5 (or close to) Poisson's ratio, as well as modelling water using Tait equation and so forth. While the loading regime does not necessarily warrant the consideration of high pressure loading, the choice of this model for the axoplasm and extra cellular matrix allows for straightforward extension of the model to such regimes.

In reality, brain white matter is tightly packed with neurons and glial cells, whereas neuronal axons are encased within multiple long myelinated sections with short gaps in between (the nodes of Ranvier). Studying how neurons mechanically respond to external loadings (especially acoustic pressures) at the cellular level is of direct relevance for an increased understanding the

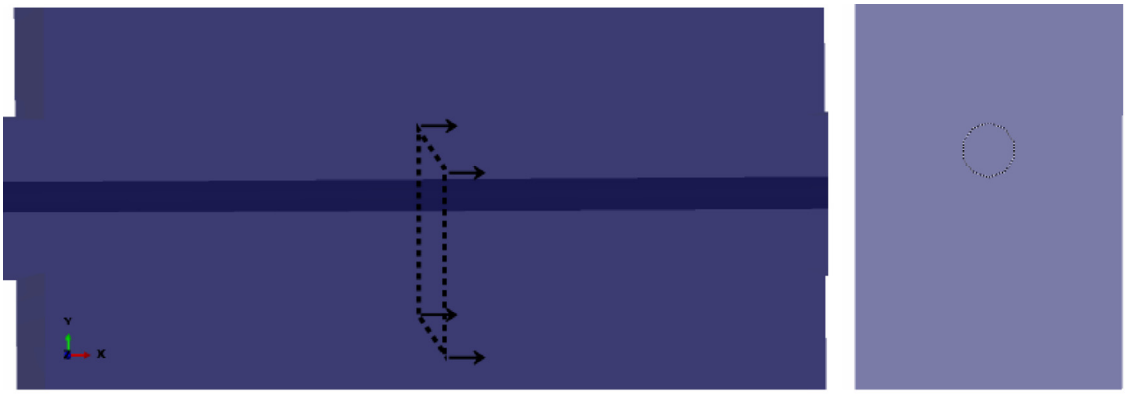

(a) Axon unloaded

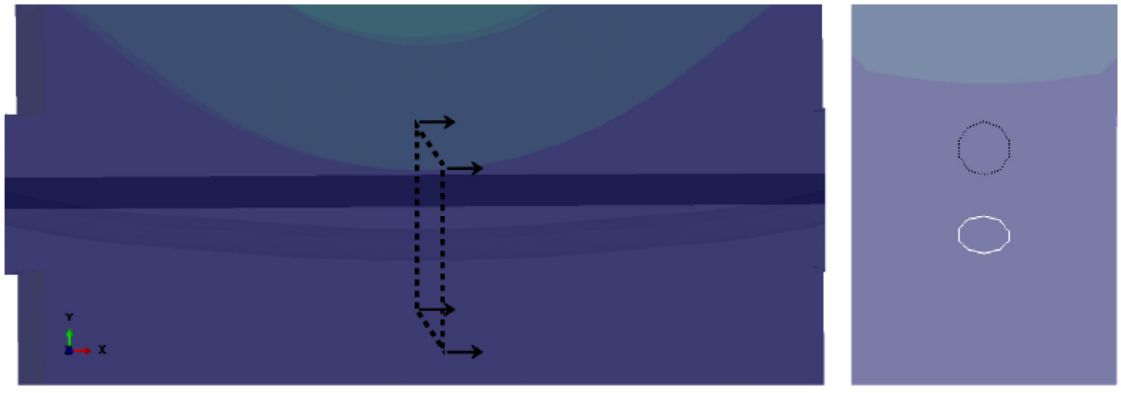

(b) Axon in compression phase

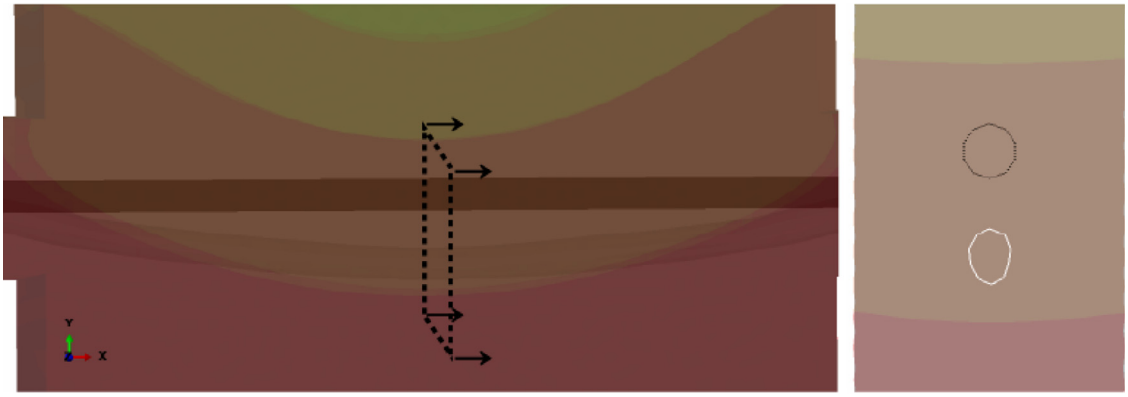

(c) Axon in rarefaction phase

Fig. 6. Periodical deformation of cross section of the axon for NF= 450 kHz, PRF= 500 Hz, SIA = 90°. The right insets show the middle cross section of the axon; black dotted line: undeformed cross section, white: deformed cross section. (a): The axon is unloaded (no pressure wave), therefore no deformation occurs (0 ms). (b): The axon is in the compression phase of the pressure wave, therefore the cross section is pushed downwards, vertically compressed and laterally stretched (0.445 ms). (c): The axon is in the rarefaction phase of the pressure wave, therefore the cross section is vertically stretched and laterally compressed (0.668 ms).

action mechanism of TUS. Unfortunately, such information is not readily accessible by current experimental techniques. For this reason, numerical models have been proposed to investigate the deformation/vibration of neurons under mechanical loadings. These numerical models can be generally classified into three categories. The first category include mathematical models of lipid bilayer membrane leaflets with an embedded ultrasound-induced bubble [29,39,82,83]. In these models, idealised geometries are used to model the membrane leaflets, whereas its oscillation is governed by the modified Rayleigh-Plesset bubble dynamics. Being phenomenological in nature, this type of models can conceptually describe the local vibration of neuron membrane in its deformed configurations upon the application of ultrasound and potentially describe the resulting subcellular, intra-membrane changes. However, it cannot distinguish acoustic waves incoming from different SIAs, nor is it able to model other types of mechanical stimulations, such as in Ref. [84] and [85]. In addition, further development of these models to work on more complicated geometries (such as realistic/3D geometries) is not straightforward. The second category include finite element models of single cell of either idealised or realistic geometries under mechanical loadings [31,40,61,62,86]. One advantage of this type of models is their ca-

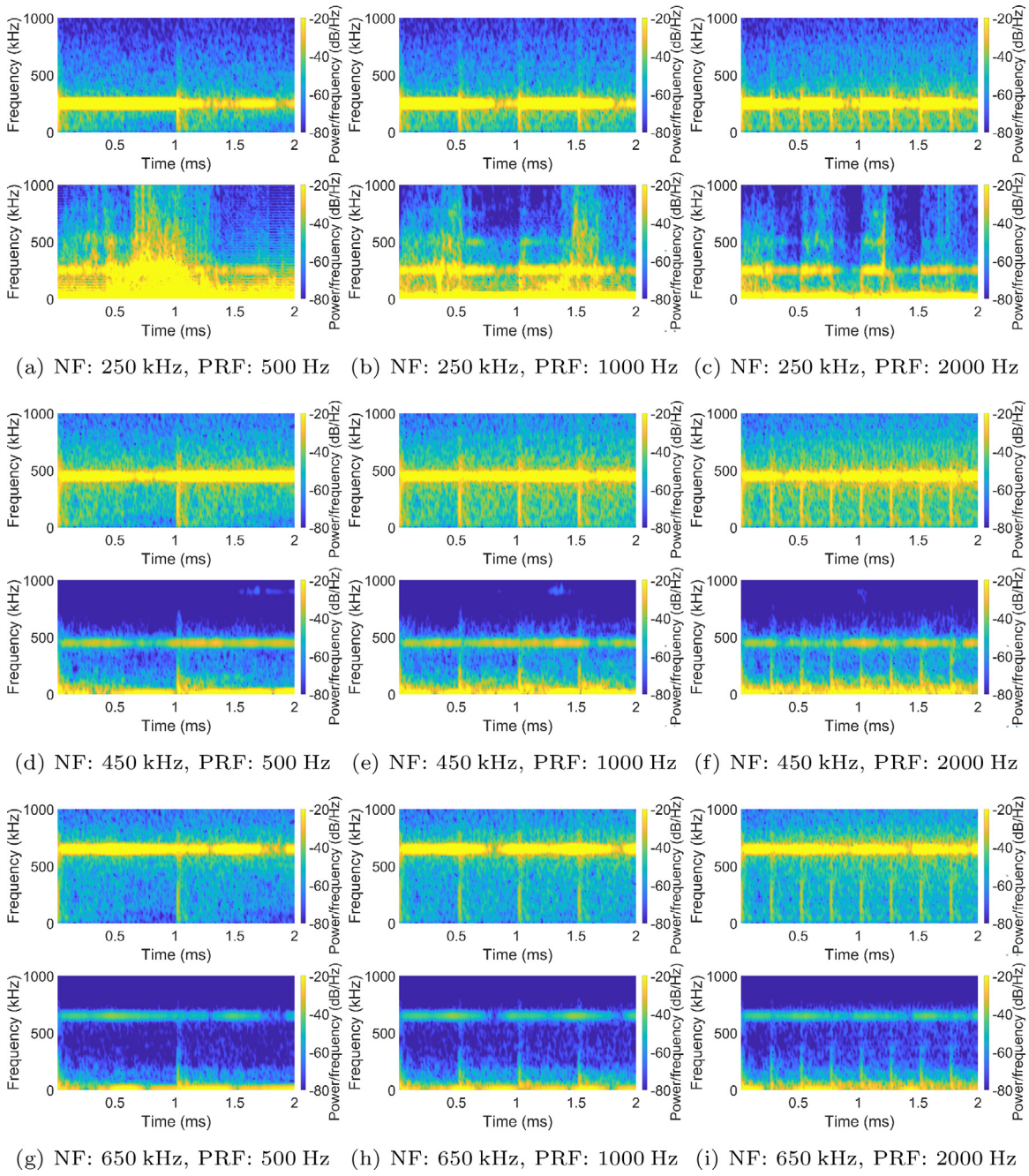

Fig. 7. Spectrogram analyses of the local pressure waves in the upper row, and axonal vibration (characterised by the alteration of axon middle section diameters) in the lower row. The local pressure waves are computed in the macroscopic model under different combinations of natural frequencies (NFs) and pulse repetition frequencies (PRFs), as shown in Figure 4.

pability to explicitly capture the mechanical response of a single neuron cell under complex loading conditions. For example, Ref. [40] and [31] showed that the stimulation of the axon end with a train of pulsed longitudinal mechanical waves mimicking low frequency pulsed ultrasound also induces a series of accompanying transverse waves that locally flex the membrane due to the Poisson effect. While this type of models is easy to develop for further evolutions, they lack scalability and often neglect the interactions between neurons and their surrounding ECM/neurons. The third category consists of finite element models simulating the mechanical behaviour of a (potentially homogenised) group of neurons embedded within a representative volume such as a collagenous matrix under either quasi-static or low-rate dynamic loadings [87–91]. In these models, geometries of the simulated cell are either idealised or constructed from cell image stacks. Instead of being applied on the cells directly, loadings are usually applied on the surrounding matrix. Simulation results show that stress concentration/strain amplification can be usually observed at certain locations on the neurons. The direct advantage of this category of models is that they incorporate the influence of ECM heterogeneity (including other neighbouring cells) in quantifying the mechanical behaviour of each single cell. However, this is achieved at the expense of a much coarser modelling of the details due to the model complexity. This limits their ability to model lower-level phenomena such as membrane waves and membrane vibrations, which are predictable in the first two categories of models. The MiM follows

the approach of the second category but incorporates the fluid-solid interactions between the membrane and the ECM, as well as between the membrane and the axoplasm. This is achieved by modelling the membrane as a Lagrangian shell structure coupled to the inner axoplasm and outer ECM, both of which are modelled using an Eulerian mesh. It is, however, worth emphasising that this modelling choice does not imply that the axons are moving freely in the surrounding environment: the ECM and axoplasm both constrain the axonal membrane through their consitutive and contact relationships.

4.3. Determination of the optimised sonication parameters

A pulsed ultrasound stimulus can be characterised by five main parameters: its NF, intensity, stimulation duration, PRF and DC. Each of these parameters may have a strong effect on the stimulation outcome [4]. For example, both experimental and numerical studies of ultrasound-induced neurostimulation suggest that a lower bound threshold of acoustic intensity may exist for successful low intensity TUS neuromodulation. Taking the upper bound threshold approved by the Food and Drug Administration for diagnostic usage of ultrasound for adults [92], which is approximately $38 - 47.5\,\mathrm{W/cm^2}$ of I_{SPPA} at the focal zone (approximated by multiplying $190\,\mathrm{W/cm^2}$ with the attenuation rate), indicates that there may be one optimal I_{SPPA} between the two bounds associated with the best modulation outcome. Two approaches are usually followed to determine the best sonication parameters. The first one consists in exploring a range of sonication parameters which can successfully cause stimulative effects while minimising the acoustic intensity deposition. For example, Ref. [93] found that TUS elicits rat motor responses in a limited range of sonication parameters, in which $1 - 5$ ms of tone-burst duration, 50% of DC (as opposed to 30% and 70%), and 300 ms of sonication duration (as opposed to 200 ms and 400 ms), at 350 kHz NF (as opposed to 650 kHz) together result in the lowest acoustic intensity. The second approach consists in seeking a combination of sonication parameters which can result in the highest efficiency during stimulation, which is usually assessed by the neuron electrophysiological responses, e.g., through analysis of electromyogram and electroencephalographic signals. For instance, using mouse somatomotor response, Ref. [27] reported that stimulation success increases as a function of both acoustic intensity and stimulation duration, and a successful stimulation results from the integration of an adequately strong stimulus amplitude over a time interval of $50 - 150$ ms. In the case of pulsed ultrasound, success rate increases with the increase of DC. Ref. [28] found that specific sonication parameters outperformed others in modulating ovine regional brain activities, with the highest response rate generally occurring at 70% DC (as opposed to 30%, 50% and 100%), shorter tone-burst duration (0.5 ms as opposed to $1 - 3$ ms) and lower I_{SPPA} ($15.8\,\mathrm{W/cm^2}$ as opposed to $18.2\,\mathrm{W/cm^2}$). Our study generally follows the first approach, and the endpoint of the simulations are energy rate densities. Strictly speaking, this paradigm lacks the final prediction of the electrophysiological activities of the neurons (i.e., it does not predict whether a certain dose of ultrasound intensity will successfully induce neuron modulation or not). This can be achieved by two means: 1) by knowing which mechanism(s) links the mechanical energy to electrophysiological alterations, something that is currently unknown; or 2) by experimental validation able to quantify energetic contributions consistently across specimens, a task similarly marred with obstacles.

In spite of the difficulty, numerical studies have been proposed to model ultrasound-induced cell membrane polarisation/action potential. These models are thus built on different underlying modulation assumptions (such as direct flexoelectricity or intramembrane cavitation excitation [29,39,94]), and are often restricted to 1D. Our framework sits above the need for a choice of a candidate mechanism as it is solely focussed on energy. It can, though, be used to follow the second approach, i.e., quantifying the efficiencies of different combinations of sonication parameters by the neuronal activities that they can induce in terms of energetic transfer to the axon. This, however, requires the consideration of additional experimental work focussed on the ultrasound modulation efficacy of the same monkey from whom the head images are obtained, at different levels of intensities while fixing other sonication parameters, with the placement of the transducer at the same location. In view of the difficulty associated to doing these experiments, this effort is beyond the scope of this work. Some general observations can nevertheless be drawn. The current literature seems to be reaching a consensus in that a lower frequency can increase the efficacy, while an increased frequency requires an increased intensity to achieve equivalent efficacy [93,95,96]. Discrepancies still exist on the question of efficacy comparison between the use of pulsed sonication and its equivalent continuous sonication [27,93]. Based on the current literature, achieving the highest stimulation efficacy relies on the careful optimisation of fundamental sonication parameters [4,28,97]: the NF which cannot be allowed to be too high along with a conjugated intensity, a high PRF which produces hundreds of pulses during the sonication duration, and an intermediate level DC (30% – 60%)[1]. As such, we have selected sonication parameters accordingly, including NF (250 kHz, 450 kHz and 650 kHz), pressure (1.35 MPa), stimulation duration (2 ms), PRF (500 Hz, 1000 Hz and 2000 Hz) as well as DC (50%). However, one must be aware that these protocols may be neuron-type dependent [99], and may also depend on the position of the transducer as well as the brain region to be stimulated. Many unknowns exist and more coupled experimental-numerical studies are clearly needed to test these hypotheses.

4.4. Thermodynamic implications of the model

In our modelling framework, we use PAEERD and PAVERD to quantify the energy rate densities which are either locally absorbed or dissipated by the axon under TUS actions. This is a more realistic interpretation of the energy states of the neuron cells themselves during TUS, than quantifying it solely with 'intensity', which actually describes the energy carried by the acoustic waves, and not the energy states of individual neurons. According to our simulation results, the value of PAEERD is usually at least two orders of magnitude higher than that of PAVERD. This indicates that most of the energy carried by the pressure wave is transferred elastically rather than dissipated by the cell's viscosity. Nevertheless, this dissipation cannot be ignored, as its accumulation contributes to the attenuation of the acoustic waves through the brain tissue which can be quite significant when the propagation path is long.

In high intensity focused ultrasound (HIFU) ablation, a non-significant part of the kinetic energy of the sound wave is absorbed by the brain tissue and converted into thermal energy. These two coupled forms of energies conjointly induce both rapid tissue temperature rise and micro-bubble cavitation in the focal zone, eventually leading to coagulative necrosis [100–103]. This is commonly regarded as the main underlying mechanism for HIFU. However, for low intensity ultrasound, these physical effects do not seem likely to occur, as the temperature rise in low intensity ultrasound is minimal [2,5,104] and cavitation is prone to occur more easily under high energy-level acoustic environment [105]. In order to have a better quantitative understanding of the energy states of a neuron when subjected to low intensity pulsed ultrasound

[1] Skin burn was previously observed at 60% [98].

with clinically relevant parameters, we mapped here the axon mechanical energy state back to the MaM stimulation sonication parameters (whose ranges were taken from existing monkey experimental studies). To have a better understanding of the relationships between the neuron energy states and the alteration of cell functionality, it is worth comparing our simulation outcomes with the strength of acoustic intensity at the cellular level. In the literature, studies on TUS stimulation on human brains have demonstrated that values of I_{SPPA} in the focal zone approximately between $0.1 - 6.6\,W/cm^2$ are able to induce brain activity alterations [70,106–108]. Comparing with the incident I_{SPPA} used at the acoustic source, this indicates an attenuation of $75 - 80\%$ of the intensity on average during propagation. Studies on non-human primate brains show that similar I_{SPPA} values in the targeted region are required to causally modulate monkey behaviour [47,48,109,110]. In addition, animal models of other species also use I_{SPPA} within a range comparable to humans' for successful sonication-induced stimulation of the animal's primary somatomotor and visual areas [27,28,94,111–113]. In most of these studies, only values of I_{SPPA} at the acoustic source were provided. Nevertheless, since these animal species usually have a head size smaller than humans' and a thinner skull, the associated attenuation rate can be expected to be lower than that of human, i.e., $< 75\%$. As a result, I_{SPPA} in the focal region can be estimated using an attenuation rate of 75%. At the neuron scale, it has been shown in both experimental studies and numerical models that ultrasound with I_{SPPA} falling in this range can alter the response behaviour of specific channels and modulate its channel current by different mechanical effects, including cavitation induction and mechanosensitive ion channel TRAAK activation through increasing membrane tension [16,38,39,114]. Nevertheless, values of I_{SPPA} beyond this range in the focal zone used for successful modulation of nerve circuits have also been documented in the literature [19,115,116]. Comparing with the results of all studies above, the values of PAEERD at the membrane surface computed in our simulations also fall within this range for cases of $SIA = 90°C$ and $SIA = 45°C$. This not only substantiates that our proposed quantity PAEERD is closely related to the commonly used I_{SPPA}, but also corroborates the fact that the sonication protocols that are commonly used in the literature can cause changes in the energy states in the neurons which might alter its functionalities due to mechanically related mechanisms, resulting in certain neuromodulation effects. In addition, it is worth noting that in the cases of $SIA = 0°C$, the level of PAEERD is much lower than in the cases of $SIA = 90°C$ and $SIA = 45°C$. Apart from inspecting the acoustic energy that is transformed into neuron kinetic energy, our study also examined the energy that has been locally dissipated due to viscous effects. To the best knowledge of the authors, this is the first study in the literature doing so. Such approach has important implications. Indeed, while PAEERD directly relates to stored mechanical energy (arising from the transfer of mechanical energy from the ultrasound wave's kinetic energy to the axonal membrane's elactic energy), PAVERD relates to dissipated energy (arising from the transfer of mechanical energy from the ultrasound wave's kinetic energy to the axonal membrane's heat—or thermal energy—from viscous effects). As discussed earlier, though low energy TUS are not believed to contribute to significant temperature rise, it cannot be excluded that reversible minute thermal fluctuations could not lead to functional alterations. More importantly, this observation bears resemblance with some recent work of the authors demonstrating experimentally how individual neurons could alter their electrophysiological properties under dynamic loading at ultrasonic frequencies [117]. In this work, we concluded that energetic contributions and exchanges were key to a scalable systemic understanding of TUS. Here, viscosity per se is merely a phenomenological formulation indicating a net "loss" of stored elastic energy, but could actually be—akin to the Onsager's variational principle—represent a transfer of energy from a mechanical nature to another nature. It could be thermal, as often formulated, but could also be thought of as a transfer into biochemical or electrophysiological energy through phase changes or ion channel activation [117]. Again, such consideration allows for a scalable understanding of TUS effects; namely energetic transfer from mechanical to functional, something not achievable with other approaches. Analysing in more depths whether stored mechanical energy or transferred energy (e.g., thermal, biochemical or electrophysiological), or a combination, is what leads to the functional change of individual neurons will require more experimental work for proper validation.

4.5. Vibration analysis of the neurons

In this study, we also analysed the vibration patterns of the axons under pressure waves using frequency spectrograms and compared the results with those of triggering acoustic waves themselves. Our results show that the vibration of the axons is dominated by the NF of the pressure waves, and influenced potentially by the natural resonance frequency of the axon-ECM complex. The PRF of the pressure waves did not have any discernible effect on their vibration patterns. To the authors' best knowledge, this study is the first study analysing the vibration patterns of a neuron under realistic acoustic pressure waves. The methodology used in our study can be directly leveraged to investigate whether the effect of neuromodulation of ultrasound is related to certain vibration frequencies/patterns/modes of these neuronal cells.

4.6. Future sophistications of the framework

In computational simulations, modelling dynamic response of inhomogeneous materials under high frequency vibrations requires very small time steps and space discretisation, especially for a complex modelling framework like ours which contains millions of elements and voxels and includes fluid-solid interaction. This results in an enormous increase in computational cost even when using cluster computing, therefore limiting the total duration of the dynamic event that can be simulated. In our simulations, the highest acoustic frequency is 650 kHz. For this reason, we had to limit the total duration of our simulations to 2 ms, i.e., four full pulse repetitions given a 2 kHz PRF. The sonication duration of a typical TUS neuromodulation usually lasts for at least hundreds of milliseconds, and can be up to several seconds, or even minutes [7,118,119]. This indicates that our modelling framework only simulates the first small portion of the potential total duration of a typical TUS neuromodulation, and the PAEERD and PAVERD measured in the simulations only represent the very early state of the energy levels of a neuron during a TUS neuromodulation. Studies have suggested that it may be in fact the longer temporal action of the acoustic wave which has the neuromodulatory effect [30,118], and in this case, a much longer simulation which can model a TUS neuromodulation of at least one second duration will be more appropriate in the future. Furthermore, while PAEERD was observed to reach a steady state (the value provided is the one at the end of the simulation), PAVERD, by its dissipative nature, was observed to increase (quasi linearly) with time, thus potentially justifying the need for longer simulations—or at least linear extrapolation—if one considers the transfer of energy from mechanics to electrophysiology as the leading neuromodulation mechanism in a longer modulation time window.

Apart from extending the simulation duration, our modelling framework can be further sophisticated in three other directions. The first direction is to use a realistic geometry of neuron or axon similar to the one used in Ref. [86] instead of the idealised geometry used here in the MiM, and to use diffusion tensor

imaging to map realistic white matter tractography in the brain [45], rather than pre-assigned axon orientations. Similarly, other patient-specific head models, and more accurate skull morphologies and microstructural details can be developed to obtain more accurate and personalised results. The second direction is to incorporate a 3D electrophysiological model simulating action potential propagation in cells and an electromechanical coupling model simulating mechanically induced membrane depolarisation. For the electrophysiological model, classical models such as the Hodgkin-Huxley [120], FitzHugh-Nagumo [121] or Hindmarsh-Rose models [122] could be used, whereas for the electromechanical coupling model, models simulating flexoelectricity, acoustic-induced membrane cavitation and/or acoustic-induced ion channel activation can be used. The third direction is to go further down to the subcellular scale and transform the proposed approach into a three-scale modelling framework, similar to the work done by Ref. [123] and [124]. In fact, the authors have already conducted molecular dynamics studies on membrane deformations in response to external loads/membrane pore sealing at the molecular level, for example, see Ref. [125,126]. While linking our MiM model to these membrane molecular dynamics models could be seen as straightforward, it faces a few difficulties. The first one is that the time scale might end up being drastically different (molecular dynamics considering much smaller time scales). Secondly, such approach would mean that one is required to focus on molecular systems assumed to be the main drivers of the coupling between mechanics and electrophysiological alteration (i.e., which subcellular and intra-membrane events occur, e.g., changes of membrane ion channels configurations or membrane protein vibrations under ultrasonic forces), something that this work aims at avoiding. Instead, this study stops at the cellular scale (and in particular axons) with the aim to investigate energetic quantities, which we argue are the only multiscale quantities available to multiphysics. One must additionally note that the computational cost of the current modelling framework is already expensive, and future sophistications including 3D electrophysiological and electromechanical coupling models or the development into a three-scale modelling framework would all further increase the computational complexity. Our modelling framework also has the advantage to “speak the same language” as current experimental studies focussed on identifying cell-level energy states and analysing acoustics-driven cell vibration informations in the regions of interest under specific sonication protocol and settings.

5. Conclusion

While low intensity, low frequency TUS has gradually emerged as a novel technique for clinical non-invasive neuromodulation, its underlying modulation mechanisms are still unclear, further complicating the identification of an optimum sonication protocol for a given configuration. From a thermodynamic standpoint, ultrasound-induced nerve activity alteration can be attributed to the mechanical energy and/or entropy/enthalpy conversions occurring at the cellular (or possibly sub-cellular) scale. Building on this, this study proposes a multiscale modelling framework to examine the energy states of neuronal axons under TUS. Using this framework, we computed elastically stored and viscously dissipated energy density rates of the axonal membrane and mapped them back against the sonication parameters of the stimulating waves at the organ level. We also analysed the vibration patterns of the axons under these stimulating waves. Comparing with literature simulation predictions and experimental results, we concluded that the proposed modelling framework constitutes a promising predicting platform for the identification of the optimised acoustic parameters to be used in TUS neuromodulation for safer and successful treatments of neurological disorders. Finally, the two-scale approach is suitable for a personalisation of the upper scale framework accounting exactly for skull geometries (e.g., skull thickness/shape variations in one patient and/or between patients) and tissue morphologies and properties (e.g., future evolution of the model including differentiation between pyramidal neurons, interneurons, glial cells composition), which could directly feed into personalised clinical approaches for TUS treatment.

Data accessibility statement

All data is provided in full in the results section of this paper with raw simulation data available upon request.

Rights retention statement

This research was funded in whole, or in part, by the EPSRC Healthcare Technologies Challenge Award EP/N020987/1. For the purpose of Open Access, the author has applied a CC BY public copyright licence to any Author Accepted Manuscript version arising from this submission.

Declaration of Competing Interest

The authors declare that they have no known competing financial interests or personal relationships that could have appeared to influence the work reported in this paper.

Acknowledgement

The authors acknowledge funding from the EPSRC Healthcare Technologies Challenge Award EP/N020987/1. JS is funded by the LabEx CORTEX-Universite de Lyon.

References

[1] W.J. Tyler, Y. Tufail, M. Finsterwald, M.L. Tauchmann, E.J. Olson, C. Majestic, et al., Remote excitation of neuronal circuits using low-intensity, low-frequency ultrasound, PLoS ONE 3 (10) (2008), doi:10.1371/journal.pone.0003511.
[2] H. Baek, K.J. Pahk, H. Kim, A review of low-intensity focused ultrasound for neuromodulation, Biomedical Engineering Letters 7 (2) (2017) 135–142, doi:10.1007/s13534-016-0007-y.
[3] P.-C. Chu, H.-L. Liu, H.-Y. Lai, C.-Y. Lin, H.-C. Tsai, Y.-C. Pei, Neuromodulation accompanying focused ultrasound-induced blood-brain barrier opening, Scientific Reports 5 (1) (2015), doi:10.1038/srep15477.
[4] J. Kubanek, Neuromodulation with transcranial focused ultrasound, Neurosurgical Focus 44 (2) (2018) E14, doi:10.3171/2017.11.focus17621.
[5] J. Blackmore, S. Shrivastava, J. Sallet, C.R. Butler, R.O. Cleveland, Ultrasound neuromodulation: A review of results, mechanisms and safety, Ultrasound in Medicine & Biology 45 (7) (2019) 1509–1536, doi:10.1016/j.ultrasmedbio.2018.12.015.
[6] L.d. Biase, E. Falato, V.D. Lazzaro, Transcranial focused ultrasound (tFUS) and transcranial unfocused ultrasound (tUS) neuromodulation: From theoretical principles to stimulation practices, Frontiers in Neurology 10 (2019), doi:10.3389/fneur.2019.00549.
[7] P. Wang, J. Zhang, J. Yu, C. Smith, W. Feng, Brain modulatory effects by low-intensity transcranial ultrasound stimulation (TUS): A systematic review on both animal and human studies, Frontiers in Neuroscience 13 (2019), doi:10.3389/fnins.2019.00696.
[8] B. Feng, L. Chen, S.J. Ilham, A review on ultrasonic neuromodulation of the peripheral nervous system: Enhanced or suppressed activities? Applied Sciences 9 (8) (2019) 1637, doi:10.3390/app9081637.
[9] T. Kim, C. Park, P.Y. Chhatbar, J. Feld, B.M. Grory, C.S. Nam, P. Wang, M. Chen, X. Jiang, W. Feng, Effect of low intensity transcranial ultrasound stimulation on neuromodulation in animals and humans: An updated systematic review, Frontiers in Neuroscience 15 (2021), doi:10.3389/fnins.2021.620863.
[10] T. Zhang, N. Pan, Y. Wang, C. Liu, S. Hu, Transcranial focused ultrasound neuromodulation: A review of the excitatory and inhibitory effects on brain activity in human and animals, Frontiers in Human Neuroscience 15 (2021), doi:10.3389/fnhum.2021.749162.
[11] J. Lim, H.-H. Tai, W.-H. Liao, Y.-C. Chu, C.-M. Hao, Y.-C. Huang, C.-H. Lee, S.-S. Lin, S. Hsu, Y.-C. Chien, D.-M. Lai, W.-S. Chen, C.-C. Chen, J.-L. Wang, ASIC1a is required for neuronal activation via low-intensity ultrasound stimulation in mouse brain, eLife 10 (2021), doi:10.7554/elife.61660.
[12] L. Shi, Y. Jiang, N. Zheng, J.-X. Cheng, C. Yang, High-precision neural stimulation through optoacoustic emitters, Neurophotonics 9 (03) (2022), doi:10.1117/1.nph.9.3.032207.

[13] A. Vasan, J. Orosco, U. Magaram, M. Duque, C. Weiss, Y. Tufail, S.H. Chalasani, J. Friend, Ultrasound mediated cellular deflection results in cellular depolarization, Advanced Science 9 (2) (2021) 2101950, doi:10.1002/advs.202101950.
[14] J. Kubanek, J. Shi, J. Marsh, D. Chen, C. Deng, J. Cui, Ultrasound modulates ion channel currents, Scientific Reports 6 (1) (2016), doi:10.1038/srep24170.
[15] J. Kubanek, P. Shukla, A. Das, S.A. Baccus, M.B. Goodman, Ultrasound elicits behavioral responses through mechanical effects on neurons and ion channels in a simple nervous system, The Journal of Neuroscience 38 (12) (2018) 3081–3091, doi:10.1523/jneurosci.1458-17.2018.
[16] Z. Lin, X. Huang, W. Zhou, W. Zhang, Y. Liu, T. Bian, L. Niu, L. Meng, Y. Guo, Ultrasound stimulation modulates voltage-gated potassium currents associated with action potential shape in hippocampal CA1 pyramidal neurons, Frontiers in Pharmacology 10 (2019), doi:10.3389/fphar.2019.00544.
[17] Z. Qiu, J. Guo, S. Kala, J. Zhu, Q. Xian, W. Qiu, G. Li, T. Zhu, L. Meng, R. Zhang, H.C. Chan, H. Zheng, L. Sun, The mechanosensitive ion channel piezo1 significantly mediates in vitro ultrasonic stimulation of neurons, iScience 21 (2019) 448–457, doi:10.1016/j.isci.2019.10.037.
[18] Z. Qiu, S. Kala, J. Guo, Q. Xian, J. Zhu, T. Zhu, X. Hou, K.F. Wong, M. Yang, H. Wang, L. Sun, Targeted neurostimulation in mouse brains with non-invasive ultrasound, Cell Reports 32 (7) (2020) 108033, doi:10.1016/j.celrep.2020.108033.
[19] Z. Cui, D. Li, Y. Feng, T. Xu, S. Wu, Y. Li, A. Bouakaz, M. Wan, S. Zhang, Enhanced neuronal activity in mouse motor cortex with microbubbles' oscillations by transcranial focused ultrasound stimulation, Ultrasonics Sonochemistry 59 (2019) 104745, doi:10.1016/j.ultsonch.2019.104745.
[20] P.S. Balasubramanian, Characterization of SH-SY5y neurons subject to 92khz ultrasound stimulation, International Journal of Morphology 39 (4) (2021) 1109–1115, doi:10.4067/s0717-95022021000401109.
[21] S. Yoo, D.R. Mittelstein, R.C. Hurt, J. Lacroix, M.G. Shapiro, Focused ultrasound excites cortical neurons via mechanosensitive calcium accumulation and ion channel amplification, Nature Communications 13 (1) (2022), doi:10.1038/s41467-022-28040-1.
[22] E. Sassaroli, N. Vykhodtseva, Acoustic neuromodulation from a basic science prospective, Journal of Therapeutic Ultrasound 4 (2016) 17, doi:10.1186/s40349-016-0061-z.
[23] A. Fomenko, C. Neudorfer, R.F. Dallapiazza, S.K. Kalia, A.M. Lozano, Low-intensity ultrasound neuromodulation: An overview of mechanisms and emerging human applications, Brain Stimulation 11 (6) (2018) 1209–1217, doi:10.1016/j.brs.2018.08.013.
[24] A. Jerusalem, Z. Al-Rekabi, H. Chen, A. Ercole, M. Malboubi, M. Tamayo-Elizalde, L. Verhagen, S. Contera, Electrophysiological-mechanical coupling in the neuronal membrane and its role in ultrasound neuromodulation and general anaesthesia, Acta Biomaterialia (2019), doi:10.1016/j.actbio.2019.07.041.
[25] M.D. Menz, P. Ye, K. Firouzi, A. Nikoozadeh, K.B. Pauly, P. Khuri-Yakub, S.A. Baccus, Radiation force as a physical mechanism for ultrasonic neurostimulation of the ex vivo retina, The Journal of Neuroscience 39 (32) (2019) 6251–6264, doi:10.1523/jneurosci.2394-18.2019.
[26] A. Lozano, A. Fomenko, Neuromodulation and ablation with focused ultrasound – toward the future of noninvasive brain therapy, Neural Regeneration Research 14 (9) (2019) 1509, doi:10.4103/1673-5374.255961.
[27] R.L. King, J.R. Brown, W.T. Newsome, K.B. Pauly, Effective parameters for ultrasound-induced in vivo neurostimulation, Ultrasound in Medicine & Biology 39 (2) (2013) 312–331, doi:10.1016/j.ultrasmedbio.2012.09.009.
[28] K. Yoon, W. Lee, J.E. Lee, L. Xu, P. Croce, L. Foley, S.-S. Yoo, Effects of sonication parameters on transcranial focused ultrasound brain stimulation in an ovine model, PLOS ONE 14 (10) (2019) e0224311, doi:10.1371/journal.pone.0224311.
[29] T. Lemaire, E. Neufeld, N. Kuster, S. Micera, Understanding ultrasound neuromodulation using a computationally efficient and interpretable model of intramembrane cavitation, Journal of Neural Engineering 16 (4) (2019) 046007, doi:10.1088/1741-2552/ab1685.
[30] A. Fomenko, K.-H.S. Chen, J.-F. Nankoo, J. Saravanamuttu, Y. Wang, M. El-Baba, X. Xia, S.S. Seerala, K. Hynynen, A.M. Lozano, R. Chen, Systematic examination of low-intensity ultrasound parameters on human motor cortex excitability and behavior, eLife 9 (2020), doi:10.7554/elife.54497.
[31] H. Chen, A. Jerusalem, A framework for low-intensity low-frequency ultrasound neuromodulation sonication parameter identification from micromechanical flexoelectricity modelling, Ultrasound in Medicine & Biology 47 (7) (2021) 1985–1991, doi:10.1016/j.ultrasmedbio.2021.02.028.
[32] S. Shrivastava, K.H. Kang, M.F. Schneider, Collision and annihilation of nonlinear sound waves and action potentials in interfaces, Journal of The Royal Society Interface 15 (143) (2018) 20170803, doi:10.1098/rsif.2017.0803.
[33] S. Shrivastava, H.J. Lee, J.-X. Cheng, A thermodynamic interpretation of the stimulated raman spectroscopic signature of an action potential in a single neuron(2020). 10.1101/2020.04.20.052332
[34] T. Heimburg, A.D. Jackson, On soliton propagation in biomembranes and nerves, Proceedings of the National Academy of Sciences 102 (28) (2005) 9790–9795.
[35] C.S. Drapaca, An electromechanical model of neuronal dynamics using hamilton's principle, Frontiers in Cellular Neuroscience 9 (2015), doi:10.3389/fncel.2015.00271.
[36] R.R. Poznanski, L.A. Cacha, Y.M.S. Al-Wesabi, J. Ali, M. Bahadoran, P.P. Yupapin, J. Yunus, Solitonic conduction of electrotonic signals in neuronal branchlets with polarized microstructure, Scientific Reports 7 (1) (2017) 2746, doi:10.1038/s41598-017-01849-3.
[37] M. Mussel, M.F. Schneider, It sounds like an action potential: unification of electrical, chemical and mechanical aspects of acoustic pulses in lipids, Journal of The Royal Society Interface 16 (151) (2019) 20180743, doi:10.1098/rsif.2018.0743.
[38] M.L. Prieto, Õ. Oralkan, B.T. Khuri-Yakub, M.C. Maduke, Dynamic response of model lipid membranes to ultrasonic radiation force, PLoS ONE 8 (10) (2013) e77115, doi:10.1371/journal.pone.0077115.
[39] M. Plaksin, E. Kimmel, S. Shoham, Cell-type-selective effects of intramembrane cavitation as a unifying theoretical framework for ultrasonic neuromodulation, eneuro 3 (3) (2016), doi:10.1523/eneuro.0136-15.2016. ENEURO.0136–15.2016
[40] H. Chen, D. Garcia-Gonzalez, A. Jérusalem, Computational model of the mechano-eletrophysiological coupling in axons with application to neuromodulation, Physical Review E In press (2019).
[41] T. Tarnaud, W. Joseph, R. Schoeters, L. Martens, E. Tanghe, SECONIC: Towards multi-compartmental models for ultrasonic brain stimulation by intramembrane cavitation, Journal of Neural Engineering 17 (5) (2020) 056010, doi:10.1088/1741-2552/abb73d.
[42] T. Lemaire, E. Vicari, E. Neufeld, N. Kuster, S. Micera, MorphoSONIC: A morphologically structured intramembrane cavitation model reveals fiber-specific neuromodulation by ultrasound, iScience 24 (9) (2021) 103085, doi:10.1016/j.isci.2021.103085.
[43] T. Tarnaud, W. Joseph, R. Schoeters, L. Martens, E. Tanghe, Membrane charge oscillations during ultrasonic neuromodulation by intramembrane cavitation, IEEE Transactions on Biomedical Engineering 68 (9) (2021) 2892–2903, doi:10.1109/tbme.2021.3086594.
[44] S. Zhao, D. Liu, M. Liu, X. Luo, Y. Yuan, Theoretical analysis of effects of transcranial magneto-acoustical stimulation on neuronal spike-frequency adaptation, BMC Neuroscience 23 (1) (2022), doi:10.1186/s12868-022-00709-9.
[45] C. Felix, D. Folloni, H. Chen, J. Sallet, A. Jerusalem, White matter tract transcranial ultrasound stimulation, a computational study, Computers in Biology and Medicine 140 (2022) 105094, doi:10.1016/j.compbiomed.2021.105094.
[46] B.E. Treeby, B.T. Cox, k-wave: MATLAB toolbox for the simulation and reconstruction of photoacoustic wave fields, Journal of Biomedical Optics 15 (2) (2010) 021314, doi:10.1117/1.3360308.
[47] T. Deffieux, Y. Younan, N. Wattiez, M. Tanter, P. Pouget, J.-F. Aubry, Low-intensity focused ultrasound modulates monkey visuomotor behavior, Current Biology 23 (23) (2013) 2430–2433, doi:10.1016/j.cub.2013.10.029.
[48] N. Wattiez, C. Constans, T. Deffieux, P.M. Daye, M. Tanter, J.-F. Aubry, P. Pouget, Transcranial ultrasonic stimulation modulates single-neuron discharge in macaques performing an antisaccade task, Brain Stimulation 10 (6) (2017) 1024–1031, doi:10.1016/j.brs.2017.07.007.
[49] D. Folloni, L. Verhagen, R.B. Mars, E. Fouragnan, C. Constans, J.-F. Aubry, M.F.S. Rushworth, J. Sallet, Manipulation of subcortical and deep cortical activity in the primate brain using transcranial focused ultrasound stimulation, Neuron 101 (6) (2019) 1109–1116, doi:10.1016/j.neuron.2019.01.019.
[50] L. Verhagen, C. Gallea, D. Folloni, C. Constans, D.E.A. Jensen, H. Ahnine, L. Roumazeilles, M. Santin, B. Ahmed, S. Lehericy, M.C. Klein-Flügge, K. Krug, R.B. Mars, M.F.S. Rushworth, P. Pouget, J.-F. Aubry, J. Sallet, Offline impact of transcranial focused ultrasound on cortical activation in primates, eLife 8 (2019), doi:10.7554/elife.40541.
[51] P.-F. Yang, M.A. Phipps, A.T. Newton, V. Chaplin, J.C. Gore, C.F. Caskey, L.M. Chen, Neuromodulation of sensory networks in monkey brain by focused ultrasound with MRI guidance and detection, Scientific Reports 8 (1) (2018), doi:10.1038/s41598-018-26287-7.
[52] Z. Lin, L. Meng, J. Zou, W. Zhou, X. Huang, S. Xue, T. Bian, T. Yuan, L. Niu, Y. Guo, H. Zheng, Non-invasive ultrasonic neuromodulation of neuronal excitability for treatment of epilepsy, Theranostics 10 (12) (2020) 5514–5526, doi:10.7150/thno.40520.
[53] J. Zou, L. Meng, Z. Lin, Y. Qiao, C. Tie, Y. Wang, X. Huang, T. Yuan, Y. Chi, W. Meng, L. Niu, Y. Guo, H. Zheng, Ultrasound neuromodulation inhibits seizures in acute epileptic monkeys, iScience 23 (5) (2020) 101066, doi:10.1016/j.isci.2020.101066.
[54] K. Blaize, F. Arcizet, M. Gesnik, H. Ahnine, U. Ferrari, T. Deffieux, P. Pouget, F. Chavane, M. Fink, J.-A. Sahel, M. Tanter, S. Picaud, Functional ultrasound imaging of deep visual cortex in awake nonhuman primates, Proceedings of the National Academy of Sciences 117 (25) (2020) 14453–14463, doi:10.1073/pnas.1916787117.
[55] J. Kubanek, J. Brown, P. Ye, K.B. Pauly, T. Moore, W. Newsome, Remote, brain region–specific control of choice behavior with ultrasonic waves, Science Advances 6 (21) (2020) eaaz4193, doi:10.1126/sciadv.aaz4193.
[56] P. Pouget, S. Frey, H. Ahnine, D. Attali, J. Claron, C. Constans, J.-F. Aubry, F. Arcizet, Neuronavigated repetitive transcranial ultrasound stimulation induces long-lasting and reversible effects on oculomotor performance in non-human primates, Frontiers in Physiology 11 (2020), doi:10.3389/fphys.2020.01042.
[57] P.-F. Yang, M.A. Phipps, S. Jonathan, A.T. Newton, N. Byun, J.C. Gore, W.A. Grissom, C.F. Caskey, L.M. Chen, Bidirectional and state-dependent modulation of brain activity by transcranial focused ultrasound in non-human primates, Brain Stimulation 14 (2) (2021) 261–272, doi:10.1016/j.brs.2021.01.006.
[58] R. Bernal, P.A. Pullarkat, F. Melo, Mechanical properties of axons, Physical Review Letters 99 (1) (2007), doi:10.1103/physrevlett.99.018301.
[59] J.A. García-Grajales, A. Jérusalem, A. Goriely, Continuum mechanical modeling of axonal growth, Computer Methods in Applied Mechanics and Engineering 314 (2017) 147–163, doi:10.1016/j.cma.2016.07.032.
[60] P. Zubko, G. Catalan, A.K. Tagantsev, Flexoelectric Effect in Solids, Annual Review of Materials Research 43 (1) (2013) 387–421, doi:10.1146/annurev-matsci-071312-121634.

[61] A. Jérusalem, M. Dao, Continuum modeling of a neuronal cell under blast loading, Acta Biomaterialia 8 (9) (2012) 3360–3371, doi:10.1016/j.actbio.2012.04.039.
[62] D. Li, A. Pellegrino, A. Hallack, N. Petrinic, A. Jérusalem, R.O. Cleveland, Response of single cells to shock waves and numerically optimized waveforms for cancer therapy, Biophysical Journal 114 (6) (2018) 1433–1439, doi:10.1016/j.bpj.2017.09.042.
[63] M.A. Meyers, Dynamic Behavior of Materials, John Wiley & Sons, Inc., 1994, doi:10.1002/9780470172278.
[64] A.R. Arulpragasam, M.v.t. Wout-Frank, J. Barredo, C.R. Faucher, B.D. Greenberg, N.S. Philip, Low intensity focused ultrasound for non-invasive and reversible deep brain neuromodulation- a paradigm shift in psychiatric research, Frontiers in Psychiatry 13 (2022), doi:10.3389/fpsyt.2022.825802.
[65] Y.A. Ayala, B. Pontes, D.S. Ether, L.B. Pires, G.R. Araujo, S. Frases, L.F. Romão, M. Farina, V. Moura-Neto, N.B. Viana, H.M. Nussenzveig, Rheological properties of cells measured by optical tweezers, BMC Biophysics 9 (1) (2016), doi:10.1186/s13628-016-0031-4.
[66] T. Deffieux, E.E. Konofagou, Numerical study of a simple transcranial focused ultrasound system applied to blood-brain barrier opening, IEEE Transactions on Ultrasonics, Ferroelectrics and Frequency Control 57 (12) (2010) 2637–2653, doi:10.1109/tuffc.2010.1738.
[67] J. Mueller, W. Legon, A. Opitz, T.F. Sato, W.J. Tyler, Transcranial focused ultrasound modulates intrinsic and evoked EEG dynamics, Brain Stimulation 7 (6) (2014) 900–908, doi:10.1016/j.brs.2014.08.008.
[68] J.K. Mueller, L. Ai, P. Bansal, W. Legon, Numerical evaluation of the skull for human neuromodulation with transcranial focused ultrasound, Journal of Neural Engineering 14 (6) (2017) 066012, doi:10.1088/1741-2552/aa843e.
[69] S.-Y. Wu, C. Aurup, C.S. Sanchez, J. Grondin, W. Zheng, H. Kamimura, V.P. Ferrera, E.E. Konofagou, Efficient blood-brain barrier opening in primates with neuronavigation-guided ultrasound and real-time acoustic mapping, Scientific Reports 8 (1) (2018), doi:10.1038/s41598-018-25904-9.
[70] W. Legon, P. Bansal, R. Tyshynsky, L. Ai, J.K. Mueller, Transcranial focused ultrasound neuromodulation of the human primary motor cortex, Scientific Reports 8 (1) (2018), doi:10.1038/s41598-018-28320-1.
[71] K. Yoon, W. Lee, P. Croce, A. Cammalleri, S.-S. Yoo, Multi-resolution simulation of focused ultrasound propagation through ovine skull from a single-element transducer, Physics in Medicine & Biology 63 (10) (2018) 105001, doi:10.1088/1361-6560/aabe37.
[72] M.A. Samoudi, T.V. Renterghem, D. Botteldooren, Computational modeling of a single-element transcranial focused ultrasound transducer for subthalamic nucleus stimulation, Journal of Neural Engineering 16 (2) (2019) 026015, doi:10.1088/1741-2552/aafa38.
[73] C. Pasquinelli, H. Montanaro, H.J. Lee, L.G. Hanson, H. Kim, N. Kuster, H.R. Siebner, E. Neufeld, A. Thielscher, Transducer modeling for accurate acoustic simulations of transcranial focused ultrasound stimulation, Journal of Neural Engineering 17 (4) (2020) 046010, doi:10.1088/1741-2552/ab98dc.
[74] J. Robertson, E. Martin, B. Cox, B.E. Treeby, Sensitivity of simulated transcranial ultrasound fields to acoustic medium property maps, Physics in Medicine and Biology 62 (7) (2017) 2559–2580, doi:10.1088/1361-6560/aa5e98.
[75] A. Kyriakou, E. Neufeld, B. Werner, G. Székely, N. Kuster, Full-wave acoustic and thermal modeling of transcranial ultrasound propagation and investigation of skull-induced aberration correction techniques: a feasibility study, Journal of Therapeutic Ultrasound 3 (1) (2015), doi:10.1186/s40349-015-0032-9.
[76] Y.-B. Lu, K. Franze, G. Seifert, C. Steinhäuser, F. Kirchhoff, H. Wolburg, J. Guck, P. Janmey, E.-Q. Wei, J. Käs, A. Reichenbach, Viscoelastic properties of individual glial cells and neurons in the CNS, Proceedings of the National Academy of Sciences 103 (47) (2006) 17759–17764, doi:10.1073/pnas.0606150103. http://www.pnas.org/content/103/47/17759%5Cn http://www.ncbi.nlm.nih.gov/pubmed/17093050%5Cn http://www.pnas.org/content/103/47/17759.full.pdf
[77] J. Qiu, F.-F. Li, Identification of viscoelastic constitutive parameters of a cell based on fluid-structure coupled finite element model and experiment, Mathematical Problems in Engineering 2019 (2019) 1–13, doi:10.1155/2019/5868561.
[78] O. Wintner, N. Hirsch-Attas, M. Schlossberg, F. Brofman, R. Friedman, M. Kupervaser, D. Kitsberg, A. Buxboim, A unified linear viscoelastic model of the cell nucleus defines the mechanical contributions of lamins and chromatin, Advanced Science 7 (8) (2020) 1901222, doi:10.1002/advs.201901222.
[79] R.-J. Chen, C.-C.K. Lin, M.-S. Ju, Quasi-linear viscoelastic properties of PC-12 neuron-like cells measured using atomic force microscopy, Journal of the Chinese Institute of Engineers 34 (3) (2011) 325–335, doi:10.1080/02533839.2011.565609.
[80] P. Kollmannsberger, C.T. Mierke, B. Fabry, Nonlinear viscoelasticity of adherent cells is controlled by cytoskeletal tension, Soft Matter 7 (7) (2011) 3127–3132, doi:10.1039/c0sm00833h.
[81] H. Castellini, B. Riquelme, Study of non-linear viscoelastic behavior of the human red blood cell, 2018, (????). 10.48550/ARXIV.1810.07760
[82] B. Krasovitski, V. Frenkel, S. Shoham, E. Kimmel, Intramembrane cavitation as a unifying mechanism for ultrasound-induced bioeffects, Proceedings of the National Academy of Sciences 108 (8) (2011) 3258–3263, doi:10.1073/pnas.1015771108.
[83] M. Plaksin, S. Shoham, E. Kimmel, Intramembrane cavitation as a predictive bio-piezoelectric mechanism for ultrasonic brain stimulation, Physical Review X 4 (1) (2014) 1–10, doi:10.1103/PhysRevX.4.011004.
[84] F.J. Julian, D.E. Goldman, The effects of mechanical stimulation on some electrical properties of axons, Journal of General Physiology 46 (2) (1962) 297–313, doi:10.1085/jgp.46.2.297.
[85] S. Terakawa, A. Watanabe, Electrical Responses to Mechanical Stimulation of the Membrane of Squid Giant Axons, European Journal of Physiology 395 (1) (1982) 59–64.
[86] M. Tamayo-Elizalde, H. Chen, M. Malboubi, H. Ye, A. Jerusalem, Action potential alterations induced by single f11 neuronal cell loading, Progress in Biophysics and Molecular Biology 162 (2021) 141–153, doi:10.1016/j.pbiomolbio.2020.12.003.
[87] E. Bar-Kochba, M.T. Scimone, J.B. Estrada, C. Franck, Strain and rate-dependent neuronal injury in a 3d in vitro compression model of traumatic brain injury, Scientific Reports 6 (1) (2016), doi:10.1038/srep30550.
[88] D. Li, A. Hallack, R.O. Cleveland, A. Jérusalem, 3d multicellular model of shock wave-cell interaction, Acta Biomaterialia 77 (2018) 282–291, doi:10.1016/j.actbio.2018.04.041.
[89] M. Kazempour, M. Baniassadi, H. Shahsavari, Y. Remond, M. Baghani, Homogenization of heterogeneous brain tissue under quasi-static loading: a visco-hyperelastic model of a 3d RVE, Biomechanics and Modeling in Mechanobiology 18 (4) (2019) 969–981, doi:10.1007/s10237-019-01124-6.
[90] M. Kazempour, A. Kazempour, M. Baniassadi, Y. Remond, M. Baghani, Numerical investigation of axonal damage for regular and irregular axonal distributions, Frontiers in Mechanical Engineering 7 (2021), doi:10.3389/fmech.2021.685519.
[91] J.B. Estrada, H.C. Cramer, M.T. Scimone, S. Buyukozturk, C. Franck, Neural cell injury pathology due to high-rate mechanical loading (2021). 10.1101/2021.05.12.443823
[92] C. Pasquinelli, L.G. Hanson, H.R. Siebner, H.J. Lee, A. Thielscher, Safety of transcranial focused ultrasound stimulation: A systematic review of the state of knowledge from both human and animal studies, Brain Stimulation 12 (6) (2019) 1367–1380, doi:10.1016/j.brs.2019.07.024.
[93] H. Kim, A. Chiu, S.D. Lee, K. Fischer, S.S. Yoo, Focused ultrasound-mediated non-invasive brain stimulation: Examination of sonication parameters, Brain Stimulation 7 (5) (2014) 748–756, doi:10.1016/j.brs.2014.06.011.
[94] S.-G. Chen, C.-H. Tsai, C.-J. Lin, C.-C. Lee, H.-Y. Yu, T.-H. Hsieh, H.-L. Liu, Transcranial focused ultrasound pulsation suppresses pentylenetetrazol induced epilepsy in vivo, Brain Stimulation 13 (1) (2020) 35–46, doi:10.1016/j.brs.2019.09.011.
[95] Y. Tufail, A. Matyushov, N. Baldwin, M.L. Tauchmann, J. Georges, A. Yoshihiro, S.I.H. Tillery, W.J. Tyler, Transcranial pulsed ultrasound stimulates intact brain circuits, Neuron 66 (5) (2010) 681–694, doi:10.1016/j.neuron.2010.05.008.
[96] P.P. Ye, J.R. Brown, K.B. Pauly, Frequency dependence of ultrasound neurostimulation in the mouse brain, Ultrasound in Medicine & Biology 42 (7) (2016) 1512–1530, doi:10.1016/j.ultrasmedbio.2016.02.012.
[97] X. Wang, J. Yan, Z. Wang, X. Li, Y. Yuan, Neuromodulation effects of ultrasound stimulation under different parameters on mouse motor cortex, IEEE Transactions on Biomedical Engineering 67 (1) (2020) 291–297, doi:10.1109/tbme.2019.2912840.
[98] L. Roumazeilles, M. Schurz, M. Lojkiewiez, L. Verhagen, U. Schüffelgen, K. Marche, A. Mahmoodi, A. Emberton, K. Simpson, O. Joly, M. Khamassi, M.F.S. Rushworth, R.B. Mars, J. Sallet, Social prediction modulates activity of macaque superior temporal cortex, Science Advances 7 (38) (2021) eabh2392, doi:10.1126/sciadv.abh2392.
[99] K. Yu, X. Niu, E. Krook-Magnuson, B. He, Intrinsic functional neuron-type selectivity of transcranial focused ultrasound neuromodulation, Nature Communications 12 (1) (2021), doi:10.1038/s41467-021-22743-7.
[100] P.S. Fishman, V. Frenkel, Focused ultrasound: An emerging therapeutic modality for neurologic disease, Neurotherapeutics 14 (2) (2017) 393–404, doi:10.1007/s13311-017-0515-1.
[101] P.S. Fishman, V. Frenkel, Treatment of movement disorders with focused ultrasound, Journal of Central Nervous System Disease 9 (2017), doi:10.1177/1179573517705670. 117957351770567
[102] P. Bowary, B.D. Greenberg, Noninvasive focused ultrasound for neuromodulation, Psychiatric Clinics of North America 41 (3) (2018) 505–514, doi:10.1016/j.psc.2018.04.010.
[103] Z. Izadifar, Z. Izadifar, D. Chapman, P. Babyn, An introduction to high intensity focused ultrasound: Systematic review on principles, devices, and clinical applications, Journal of Clinical Medicine 9 (2) (2020) 460, doi:10.3390/jcm9020460.
[104] V. Ozenne, C. Constans, P. Bour, M.D. Santin, R. Valabrégue, H. Ahnine, P. Pouget, S. Lehéricy, J.-F. Aubry, B. Quesson, et al., Mri monitoring of temperature and displacement for transcranial focus ultrasound applications, NeuroImage 204 (2020) 116236, doi:10.1016/j.neuroimage.2019.116236.
[105] J. Haller, V. Wilkens, Determination of acoustic cavitation probabilities and thresholds using a single focusing transducer to induce and detect acoustic cavitation events: II. systematic investigation in an agar material, Ultrasound in Medicine & Biology 44 (2) (2018) 397–415, doi:10.1016/j.ultrasmedbio.2017.10.007.
[106] W. Legon, T.F. Sato, A. Opitz, J. Mueller, A. Barbour, A. Williams, W.J. Tyler, Transcranial focused ultrasound modulates the activity of primary somatosensory cortex in humans, Nature Neuroscience 17 (2) (2014) 322–329, doi:10.1038/nn.3620.
[107] W. Lee, H. Kim, Y. Jung, I.-U. Song, Y.A. Chung, S.-S. Yoo, Image-guided transcranial focused ultrasound stimulates human primary somatosensory cortex, Scientific Reports 5 (1) (2015) 8743, doi:10.1038/srep08743.

[108] W. Lee, H.-C. Kim, Y. Jung, Y.A. Chung, I.-U. Song, J.-H. Lee, S.-S. Yoo, Transcranial focused ultrasound stimulation of human primary visual cortex, Scientific Reports 6 (May) (2016) 34026, doi:10.1038/srep34026.
[109] E.F. Fouragnan, B.K.H. Chau, D. Folloni, N. Kolling, L. Verhagen, M. Klein-Flügge, L. Tankelevitch, G.K. Papageorgiou, J.-F. Aubry, J. Sallet, M.F.S. Rushworth, The macaque anterior cingulate cortex translates counterfactual choice value into actual behavioral change, Nature Neuroscience 22 (5) (2019) 797–808, doi:10.1038/s41593-019-0375-6.
[110] D. Folloni, E. Fouragnan, M.K. Wittmann, L. Roumazeilles, L. Tankelevitch, L. Verhagen, D. Attali, J.-F. Aubry, J. Sallet, M.F.S. Rushworth, Ultrasound modulation of macaque prefrontal cortex selectively alters credit assignment related activity and behavior, Science Advances 7 (51) (2021) eabg7700, doi:10.1126/sciadv.abg7700.
[111] S.-S. Yoo, A. Bystritsky, J.-H. Lee, Y. Zhang, K. Fischer, B.-K. Min, N.J. McDannold, A. Pascual-Leone, F.A. Jolesz, Focused ultrasound modulates region-specific brain activity, NeuroImage 56 (3) (2011) 1267–1275, doi:10.1016/j.neuroimage.2011.02.058.
[112] H. Kim, M.Y. Park, S.D. Lee, W. Lee, A. Chiu, S.-S. Yoo, et al., Suppression of EEG visual-evoked potentials in rats through neuromodulatory focused ultrasound, NeuroReport 26 (4) (2015) 211, doi:10.1097/WNR.0000000000000330.
[113] T. Bian, W. Meng, M. Qiu, Z. Zhong, Z. Lin, J. Zou, Y. Wang, X. Huang, L. Xu, T. Yuan, Z. Huang, L. Niu, L. Meng, H. Zheng, Noninvasive ultrasound stimulation of ventral tegmental area induces reanimation from general anaesthesia in mice, Research 2021 (2021) 1–13, doi:10.34133/2021/2674692.
[114] B. Sorum, R.A. Rietmeijer, K. Gopakumar, H. Adesnik, S.G. Brohawn, Ultrasound activates mechanosensitive TRAAK k+ channels through the lipid membrane, Proceedings of the National Academy of Sciences 118 (6) (2021), doi:10.1073/pnas.2006980118. e2006980118
[115] V. Colucci, G. Strichartz, F. Jolesz, N. Vykhodtseva, K. Hynynen, Focused ultrasound effects on nerve action potential in vitro, Ultrasound in Medicine & Biology 35 (10) (2009) 1737–1747, doi:10.1016/j.ultrasmedbio.2009.05.002.
[116] F. Baniasad, Transcranial focused ultrasound modulates electrical behavior of the neurons: Design and implementation of a model, Journal of Biomedical Physics and Engineering 10 (1) (2020), doi:10.31661/jbpe.v0i0.1052.
[117] M. Tamayo-Elizalde, C. Kayal, H. Ye, A. Jérusalem, Single cell electrophysiological alterations under dynamic loading at ultrasonic frequencies, Brain Multiphysics 2 (2021) 100031, doi:10.1016/j.brain.2021.100031.
[118] F. Munoz, C. Aurup, E.E. Konofagou, V.P. Ferrera, et al., Modulation of Brain Function and Behavior by Focused Ultrasound, Current Behavioral Neuroscience Reports 5 (2) (2018) 153–164, doi:10.1007/s40473-018-0156-7.
[119] B. Clennell, T.G.J. Steward, M. Elley, E. Shin, M. Weston, B.W. Drinkwater, D.J. Whitcomb, Transient ultrasound stimulation has lasting effects on neuronal excitability, Brain Stimulation 14 (2) (2021) 217–225, doi:10.1016/j.brs.2021.01.003.
[120] A.L. Hodgkin, A.F. Huxley, A Quantitative Description of Membrane Current and its Application to Conduction and Excitation in Nerves, The Journal of Physiology 117 (4) (1952) 500–544.
[121] R. FitzHugh, Impulses and physiological states in theoretical models of nerve membrane, Biophysical Journal 1 (6) (1961) 445–466, doi:10.1016/s0006-3495(61)86902-6.
[122] J.L. Hindmarsh, R.M. Rose, A model of neuronal bursting using three coupled first order differential equations, Proceedings of the Royal Society of London. Series B. Biological Sciences 221 (1222) (1984) 87–102, doi:10.1098/rspb.1984.0024.
[123] R.K. Gupta, X.G. Tan, M.R. Somayaji, A.J. Przekwas, Multiscale modelling of blast-induced TBI mechanobiology - from body to neuron to molecule, Defence Life Science Journal 2 (1) (2017) 3, doi:10.14429/dlsj.2.10369.
[124] A. Montanino, X. Li, Z. Zhou, M. Zeineh, D. Camarillo, S. Kleiven, Subject-specific multiscale analysis of concussion: from macroscopic loads to molecular-level damage, Brain Multiphysics 2 (2021) 100027, doi:10.1016/j.brain.2021.100027.
[125] L. Zhang, Z. Zhang, J. Jasa, D. Li, R.O. Cleveland, M. Negahban, A. Jérusalem, Molecular dynamics simulations of heterogeneous cell membranes in response to uniaxial membrane stretches at high loading rates, Scientific Reports 7 (1) (2017), doi:10.1038/s41598-017-06827-3.
[126] L. Zhang, Z. Zhang, M. Negahban, A. Jérusalem, Molecular dynamics simulation of cell membrane pore sealing, Extreme Mechanics Letters 27 (2019) 83–93, doi:10.1016/j.eml.2019.01.008.